Chapter 4
Producing Density and Crosswind Data from Satellite Dynamics Observations

In this chapter, the tools and models discussed in the previous chapters will be used to derive density and wind data sets from satellite dynamics observations.

In Sect. 4.1, two-line element (TLE) data on orbits of satellites and space debris objects will be used to derive density data. The main advantages of this technique are its applicability to many space objects in different orbits simultaneously, the low latency of data availability and long time span of coverage into many years in the past. A major disadvantage is the coarse temporal resolution.

In Sect. 4.2 a newly developed algorithm is presented, which can be applied to process density and crosswind data from the precise accelerometers on satellites such as CHAMP and GRACE. These satellites deliver accurate data on thermospheric density and wind speed at a very high temporal resolution and with excellent global coverage.

To conclude, Sect. 4.3 provides a more concise discussion on how software for precise orbit determination can be applied to derive density data from precise tracking data of certain scientific and operational Earth observation satellites. Only a limited number of satellites with the right tracking instrumentation is available. However, the accuracy and temporal resolution will be higher than for the TLE-derived data. This method is not extensively applied in the scientific analysis in the remainder of this thesis. However, this option is also of importance for the calibration of accelerometer measurements.

4.1 Density Determination Using Two-Line Element Data

The United States Strategic Command (USSTRATCOM) distributes orbital information on a very large number of space objects, in the form of two-line element sets (TLEs). The TLE is an extremely compact format, designed for the constraints of the information infrastructure of the 1960s, consisting of just two lines of 69 characters. Figure 4.1 shows a single TLE as an example, identifying the Kepler elements and force model parameters contained in them.

E. Doornbos, *Thermospheric Density and Wind Determination from Satellite Dynamics*,
Springer Theses, DOI: 10.1007/978-3-642-25129-0_4,

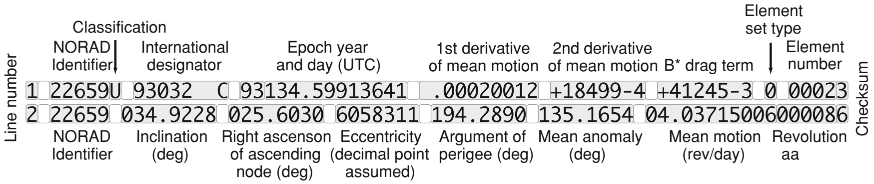

Fig. 4.1 Example two-line element set with descriptions of the data fields (after http://www.space-track.org). The TLE set shown is the first available after launch of object 22659, which was also featured in Figs. 1.2 and 1.3

These Kepler elements and force model parameters have been estimated by fitting an orbital model to space surveillance tracking data. For low Earth objects, this orbital model is implemented in the Simplified General Perturbations 4 (SGP4) propagator. SGP4 is described in detail by Hoots and Roehrich [36]. Many issues concerning its history and use in combination with TLE data are provided by Vallado et al. [82]. These two references also provide access to SGP4 source code. Vallado and Crawford [81] provide more details on the propagator's accuracy, as well as source code to use SGP4 to generate TLEs from other orbit ephemeris data.

Each of the two lines of a TLE contains the object identifier. The first TLE line contains the epoch and several force model parameters. The second TLE line contains fitted Kepler element data. The epoch is set at the last ascending equator crossing before the end of the tracking data fit span.

The first and second time derivative of the mean motion were used to model drag in an older version of the SGP model. In SGP4, these parameters are ignored, since a more sophisticated drag model is used, in which the parameter $B*$ compensates uncertainties in the ballistic coefficient of the satellite and in the density.

Note that the Kepler elements in the TLE do not represent the true orientation and shape of the satellite orbit at the provided epoch, since part of the gravity-induced orbit variations are modeled by the SGP4 propagator. The trajectories of space objects that were fitted to the observation data can only be reconstructed by the user by applying the SGP4 algorithm together with the TLE data.

The database of publicly available TLEs is updated continuously. For most objects in orbits of interest for density derivation, updates are currently provided at least daily. TLEs are also conveniently available backwards in time up to the early years of the space age, although the update frequency and accuracy for the earlier data were lower than the current level.

Figure 1.2 in the Introduction already demonstrated that there is a relation between the orbit information contained in TLEs and thermosphere density variations along the satellite's trajectory. Chapter 3 provided the mathematical description of this relation. The data processing aspects required to complete the density derivation will be provided in the following sections.

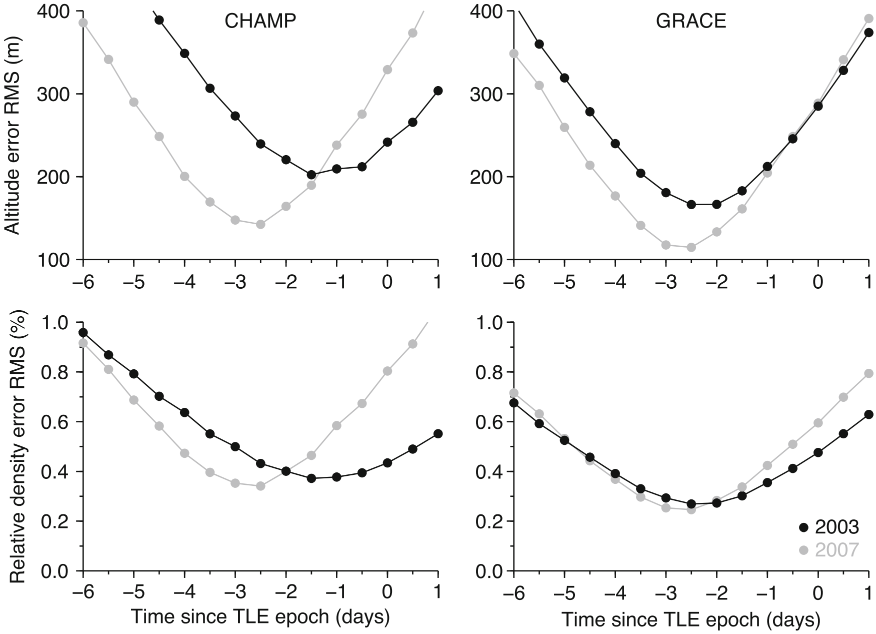

Fig. 4.2 RMS altitude error and orbit induced relative density error for CHAMP (*left*) and GRACE (*right*) TLEs

4.1.1 TLE Orbit Accuracy

Before describing the data processing strategy, it is worthwhile to have a closer look at the accuracy of the TLE orbit data, and its effect on the accuracy of density evaluation. This analysis was performed for the CHAMP and GRACE satellites, by comparing the output of the SGP4 algorithm with orbits computed using GPS tracking data. The GPS orbits used are the CHAMP rapid science orbits [42] and GRACE navigation solutions [11], which are accurate to the decimetre and few centimetre level, respectively. As we shall see, the TLE orbit errors are several orders of magnitude larger. The difference between the two orbits is therefore a good measure of the TLE orbit error.

Since the height component of the orbit is the most important for density studies, only this component is considered in the orbit error evaluation. The value for each evaluation epoch is evaluated for several surrounding TLEs. The orbit differences over two entire years, 2003 and 2007, free of orbit manoeuvres for both missions, are binned as a function of the time difference between the SGP4 evaluation epoch and the TLE epoch and plotted in the top frames of Fig. 4.2.

Densities from the NRLMSISE- 00 model were evaluated at each computed orbit position as well. The difference between the density at the TLE orbit position and the density at the precise orbit position are expressed as a percentage of the latter value. These data are processed in the same way as the orbit differences, and are plotted in the bottom panels. They can be used as a metric to evaluate the effect of TLE orbit error on density model evaluation.

According to the Figure, the TLE orbits are most accurate when evaluated 1–3 days before the TLE epoch. The accuracy is then at a level of 100–200 m, depending on the satellite and on the year. These TLE orbit errors result in minimum RMS density errors of the order 0.25–0.40%. On either side of this optimal time offset, the orbit and density errors steadily increase.

This offset of the most accurate SGP4 evaluation epoch with respect to the TLE epoch can be explained by the observation that the fitted TLE orbit is likely to be most accurate where it is strongly constrained by equal amounts of tracking data on both sides, which is often at or near the centre of the tracking data interval. On the other hand, the TLE epoch is defined at the end of this tracking data span. Under this assumption, the tracking data interval length used at Air Force Space Command to determine the TLE parameters can be estimated at about double this offset, so of the order of 2–6 days. The differences between the 2003 and 2007 averages, as well as the differences between CHAMP and GRACE suggest that the length of this tracking data span might be changed from time to time, and varies from satellite to satellite. Unfortunately, data on the tracking data span is not supplied with the TLE data, otherwise this information could be used to select the optimal TLE for orbit evaluation from the TLE time series.

According to the Figure, the GRACE TLE orbits are more accurate than the CHAMP orbits, and for both missions the orbits are more accurate in 2007 than in 2003. This is likely caused by the lower, less variable and therefore easier to model drag perturbation forces on the higher altitude GRACE compared to CHAMP and at lower solar activity in 2007 compared with 2003. A contribution to this improvement due to possible changes made in the SSN observations or the TLE data processing strategy at Air Force Space Command in between these years cannot be excluded either.

In practical applications of the SGP4 algorithm in combination with TLE data, the time difference between the evaluation epoch and the TLE epoch will often not be near the optimum value. This is due to the uncertainty in the tracking span length and the finite epoch spacing between subsequent TLEs in a time series. Fortunately, as the bottom panels of the Figure show, the density error due to TLE orbit error stays below 1%, even if the time with respect to the optimal epoch amounts to several days.

This is true for CHAMP and GRACE, and may be considered valid for satellites experiencing similar or lower levels of drag as well. However, for satellites with very low perigees, rapid changes in atmospheric density have a larger effect on the orbit, which can not always be captured in the TLE-determination spanning multiple days. The TLE orbit errors and orbit-induced density errors are likely to be much larger for such objects, and this could cause problems in the application of these data for density studies. Unfortunately, precise orbit data for such objects were not available, making it difficult to further investigate this possible limitation of the use of TLE data for thermosphere studies at this time. The future analysis of CHAMP data during the final weeks or months before its re-entry in September 2010 will be helpful in this regard.

4.1.2 History of TLE Density Processing

King-Hele [41] described the processing of TLE data for investigations of the thermosphere, but his method, which involved interpretation using an analytical atmospheric model and various other approximations, was not widely employed. One application has been the investigation of long-term trends in the thermosphere by Keating et al. [40].

Pardini et al. [67] instead use an orbit computation software package [66] to fit, in a least-squares sense, a drag coefficient to the TLE-derived orbit decay of selected satellites, using a complete model of the forces on the satellite. Their approach does not result in observations of density, but instead uses the JB2006 model, to estimate the energy accommodation coefficient parameter used in satellite aerodynamic calculations (see Sect. 3.4.3). A similar approach based on orbit determination using TLE orbits as tracking data was used by a US-Russian group of researchers [12], investigating empirical density model calibration (see Sect. 2.5).

The publication of a more efficient TLE to density processing algorithm by Picone et al. [70] has led to a wider range of research applications. These have included studies of long-term change [22, 24], a validation of density data derived from dayside limb UV airglow observations [23], an analysis of solar forcing of the thermosphere [46] and the study of empirical density model calibration [15, 16], which will be discussed in Chap. 6. The Picone et al. [70] algorithm will be described in the remainder of this section, and its results will be discussed in the next chapters.

4.1.3 Density Derivation From TLE Mean Mean Motion Data

A summary of Picone et al. [70] will be provided below. The discussion will start by covering some particulars of the TLE data and SGP4 algorithm in more detail. The presentation of the equations used to derive density from these data is followed by examples of calculation results, and a discussion of data quality and data editing aspects.

General Perturbations and Special Perturbations Orbit Determination

Picone et al. [70] start their paper by discussing the distinction between *special perturbations* and *general perturbations* orbit determination techniques. The SGP4 propagator used in TLE processing is an implementation of the general perturbations technique, in which a low order analytical solution of the perturbed equations of motion is used, and fitted to the tracking data. In contrast, the special perturbations or precise orbit determination technique involves high order numerical integration of more detailed and highly parameterised force models, and using precise measurement models to process the tracking data. This method, which is discussed in more detail in Sect. 4.3, can lead to significantly more accurate orbit and density results. On the other hand, this accuracy can only be reached for satellites equipped with suitable precise tracking instrumentation, as opposed to the ground-based radar tracking from the Space Surveillance Network employed in TLE production. In addition, the special perturbations approach requires a much larger investment in terms of force and measurement modelling effort and computation time, compared to general perturbations.

Osculating and Mean Orbital Elements

Another important distinction made in the introductory sections of Picone et al. [70] is that between osculating and mean orbital elements. Internally, the SGP4 propagator uses the analytic equations for low order orbit perturbations by Brouwer [3], and the atmospheric drag model by Lane and Cranford [43], to describe the continuously changing shape and orientation of the elliptical orbit. These are expressed in terms of osculating (or instantaneous) orbital elements, which can be directly converted to Cartesian position and velocity values at a desired epoch by applying the geometrical transformations between these two coordinate systems [63, 80].

The TLEs themselves, as shown in Fig. 4.1, contain fitted mean elements at epoch. In the fitting process, the periodic perturbations have been removed from these elements. This makes these values in the TLE data unsuitable for direct conversion to position and velocity values, either at arbitrary epochs or at the TLE epoch itself. The SGP4 propagator must always be applied to the TLE data to reconstruct the instantaneous position and velocity at its intended level of accuracy.

Derivation of the TLE to Density Processing Algorithm

Making use of the perturbation Eq. 3.38 for the semi-major axis, Picone et al. [70] show that, for the purposes of density derivation from TLEs, the focus should be on secular variations of the semi-major axis over multiple orbital revolutions. Furthermore, the paper extensively discusses the important distinction between the osculating semi-major axis a and the mean semi-major axis a_{M}, as defined by the SGP4 algorithm, from which contaminating perturbations due to the Earth's gravity field have been removed. This leaves only drag and radiation pressure to change the mean semi-major axis a_{M}. The change of this variable over time can therefore be expressed according to the sum of the perturbation Eqs. 3.38 and 3.40.

$$\frac{\mathrm{d}}{\mathrm{d}t} a_{\mathrm{M}} \cong -\frac{a_{\mathrm{M}}^2}{\mu} B \rho F v^3 + \left.\frac{\mathrm{d}a}{\mathrm{d}t}\right|_{\mathrm{R}} \tag{4.1}$$

Using Eq. 3.4, the mean semi-major axis can be converted to the mean mean motion n_{M}. This conversion is useful because n_{M} can be found directly in the TLE data.

The resulting differential equation is

$$\frac{\mathrm{d}}{\mathrm{d}t} n_{\mathrm{M}} \cong \frac{3}{2}\mu^{-\frac{2}{3}} n_{\mathrm{M}}^{\frac{1}{3}} B\rho F v^3 + \left.\frac{\mathrm{d}n_{\mathrm{M}}}{\mathrm{d}t}\right|_{\mathrm{R}} \tag{4.2}$$

When the density is large enough, radiation pressure is negligible compared to drag, and the last term in these equations can be omitted. Since this is often the case for low orbiting satellites, the derivation in Picone et al. [70] is continued under this assumption. However, at higher altitudes and low solar activity, the radiation pressure acceleration will become a major limiting factor in the accurate application of the algorithm.

Going back to the derivation, Eq. 4.2 can now be numerically integrated over the time interval between a pair of TLEs, with the epochs t_i and t_k.

$$n_{\mathrm{M}}(t_k) - n_{\mathrm{M}}(t_i) \approx \frac{3}{2}\mu^{-\frac{2}{3}} \oint_{t_i}^{t_k} n_{\mathrm{M}}^{\frac{1}{3}} B\rho F v^3 \,\mathrm{d}t \tag{4.3}$$

From this equation, the density observable can be derived. This observable is the velocity-weighted average density along the object's trajectory over the time interval between t_i and t_k. It is assigned the timestamp $t_{ik} \equiv \frac{1}{2}(t_i + t_k)$, and is defined as

$$\bar{\rho}_{\mathrm{O}}(t_{ik}) \equiv \frac{\frac{2}{3}\mu^{\frac{2}{3}}[n_{\mathrm{M}}(t_k) - n_{\mathrm{M}}(t_i)]}{\oint_{t_i}^{t_k} n_{\mathrm{M}}^{\frac{1}{3}} B F v^3 \,\mathrm{d}t} = \frac{\oint_{t_i}^{t_k} n_{\mathrm{M}}^{\frac{1}{3}} B\rho F v^3 \,\mathrm{d}t}{\oint_{t_i}^{t_k} n_{\mathrm{M}}^{\frac{1}{3}} B F v^3 \,\mathrm{d}t} \tag{4.4}$$

Next, Picone et al. [70] approximate the integrals of the ballistic coefficient B and mean motion n_{M} over the time interval by constants. For the ballistic coefficient, either an estimated value, or a model calculation (as described in Chap. 3) can be applied. The result will be an average value $\bar{B}$, which is constant over the time interval. The mean mean motion $n_{\mathrm{M}}(t)$ during the time interval is approximated by the average of the two values at the endpoints.

$$\bar{n}_{\mathrm{M}}(t_{ik}) \approx \frac{n_{\mathrm{M}}(t_i) + n_{\mathrm{M}}(t_k)}{2} \tag{4.5}$$

These substitutions result in

$$\bar{\rho}_{\mathrm{O}}(t_{ik}) \cong \frac{\frac{2}{3}\mu^{\frac{2}{3}}[n_{\mathrm{M}}(t_k) - n_{\mathrm{M}}(t_i)]}{\left[\frac{1}{2}n_M(t_i) + \frac{1}{2}n_M(t_k)\right]^{\frac{1}{3}} \bar{B} \oint_{t_i}^{t_k} F v^3 \mathrm{d}t} \tag{4.6}$$

This equation can be evaluated using the two values of n_{M} which are conveniently available from the pair of TLEs, in combination with the integrated velocities obtained from using the TLE data with the SGP4 propagator.

An equivalent velocity weighted average model density along the object's trajectory over the time interval is defined as

$$\bar{\rho}_{\mathrm{M}}(t_{ik}) \equiv \frac{\oint_{t_i}^{t_k} \rho_{\mathrm{M}} F v^3 \,\mathrm{d}t}{\oint_{t_i}^{t_k} F v^3 \,\mathrm{d}t} \tag{4.7}$$

In the evaluation of this equation, the positions of the object obtained from the SGP4 propagator are used as inputs to the density model, in order to calculate the instantaneous densities $\rho_{\mathrm{M}}(t)$ at each time step required for the numerical computation of the integral.

4.1.4 Practical TLE Processing Considerations

A number of practical considerations has to be made when processing the TLE data into density observations using the algorithm described in the previous section. These concern the selection of suitable space objects, selection and editing of their TLEs, the choice of value for the ballistic coefficients $\bar{B}$ and the choice of the integration time interval. These will be shortly discussed below.

Selection and Editing of Suitable Objects and Their TLEs

Emmert [20] defined a comprehensive series of computational tests to select suitable space objects from the space tracking catalogue, and to edit out unsuitable data from TLE time series of specific objects. For some satellites, the TLE mean motion time series shows erratic variations, because apparently SSN tracking of another object is mistakenly used. The method is intended to filter out such data as well as data for which the object apparently has unsuitable variations in cross-sectional area or undergoes orbit manoeuvres.

Ballistic Coefficients for TLE Objects

For almost all remaining suitable TLE objects, accurate information on the object geometry and attitude is not easily available, which makes it impossible to calculate the aerodynamic coefficient in detail, as described in Sect. 3.5. This problem is circumvented by assuming that the ballistic coefficient is an object-specific constant. Based on a comparison between calculations for various objects at different levels of solar activity, the errors introduced by this assumption are at the level of a few percent [14].

A value for the ballistic coefficient can be determined for each satellite by computing a long-term data over model density ratio time series, and picking the ballistic coefficient which makes the mean of the ratios equal to 1.0. Of course, the resulting TLE-derived densities will then inherit any bias present in the model that is used.

Emmert [20] uses a more sophisticated approach, by calculating the ballistic coefficient for each space object based on the minimisation of density differences between overlapping data of different objects. A single object, preferably one for which the ballistic coefficient can be calculated quite precisely, is chosen as a reference object. Emmert [20] chose the Starshine I sphere with a C_D of 2.1. However, Pilinski et al. [71] has pointed out that the Starshine spheres are not the most suitable objects for drag computations, due to the presence of attachment rings required for integration with the launch vehicle, protruding mirror plates, and cylindrical elements as part of the construction used to attach the two half-spherical elements. These deviations from a perfect aerodynamic sphere hinder a simple computation of cross-sectional area and drag coefficient. The inferred value used for the spherical area of Starshine I by Emmert [20] is about 5% smaller than the mean area of the more detailed satellite model evaluated by Pilinski et al. [71] ($A = 0.193\,\mathrm{m}^2$). Assuming that the reported mass ($m = 39.46\,\mathrm{kg}$) and assumed drag coefficient ($C_\mathrm{D} = 2.1$) for Starshine I are correct, the TLE-derived densities derived by Emmert [20] will be scaled too large by the same amount.

Although the selection of values for the satellite area and mass might at first seem a rather easy part of the drag analysis problem, the example above shows that caution is required, even for seemingly trivial satellite shapes. Values provided in scientific literature and mission documentation for other satellites could well have similar, as yet undetected, issues with their accuracy.

The data selection, editing and ballistic coefficient computation schemes of Emmert [20] ensures a level of consistency within a large set of objects, allowing for the creation of a climatological analysis [21]. However, this scheme has not yet been implemented for the work presented in this thesis. Instead, objects and ballistic coefficients were chosen based on values computed by other analysts, which were found in earlier literature [1, 2, 22, 70].

Choice of Integration Time Interval

A further choice required for the application of the algorithm by Picone et al. [70] concerns the time interval between the two TLEs with epochs t_i and t_k, from which the mean motion data are used for the computation of the density observable, using Eq. 4.6.

The irregular time interval between epochs at which consecutive TLEs are computed and delivered by Air Force Space Command is currently less than one day for most low orbiting objects. However, as shown in Sect. 4.1.1, the tracking data fit span used to generate the TLEs is selected from two days or more prior to the TLE epoch. This means that there will be some overlap in the information content of multiple TLEs when their epochs are closer together in time than the length of this fit span.

Density observations derived from such closely spaced TLE pairs show noise-like variations, apparently related to the fact that observation, processing and other numerical errors in the mean motion data are larger than the drag-induced signal. On the other hand, since the observable represents an average density, a choice for long time intervals means that short-term fluctuations in density cannot be recovered, due to the smoothing inherent in this averaging process.

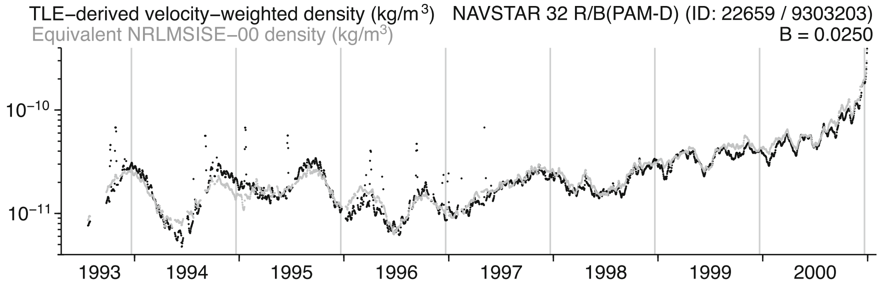

Fig. 4.3 Time series of TLE-derived velocity-weighted densities for the PAM- D object 22659, which was also featured in Figs. 1.1,1.2 and 1.2

Emmert [20] therefore selects for each TLE the first available later TLE for which the time interval is longer than three days. A maximum time interval between subsequent TLEs of 5 days is also imposed. However, such long delays between the availability of subsequent TLEs do not occur very frequently in the present data.

For this study, a different approach is used. The mean motion data from the TLEs is linearly interpolated and evaluated at regular time intervals, for instance for every integer day. This approach will be used to evaluate the influence of the integration time interval on the accuracy of the TLE-processing results in Sect. 5.3.

4.1.5 Example of TLE Density Processing

Figure 4.3 provides time series of computed values of $\bar{\rho}_O$ and $\bar{\rho}_M$, resulting from the evaluation of Eqs. 4.6 and 4.7. The values are computed for the PAM- D rocket stage that was featured earlier in Chap. 1. The general agreement between observation and model is clearly visible. Nevertheless, there are some clear outliers during the first years of the TLE-derived series, until mid-1997. These are likely due to erroneous TLE-data.

The densities derived from the TLE data will be further compared and analysed in the following chapters. In this chapter, we will move on to the presentation of other ways of deducing information on the aerodynamic interaction of the satellite with the neutral atmosphere from orbital dynamics data, starting with accelerometer data.

4.2 Density and Crosswind from Accelerometer Data

Accelerometers carried by low-Earth orbiters such as CHAMP, GRACE, GOCE and the future Swarm satellites, provide important data for improving our understanding of thermospheric density and winds. The CHAMP and GRACE missions were not designed for studies of the thermosphere; they carry accelerometers in order to allow for the removal of non-gravitational signals from measured orbit perturbations due to inhomogeneities in the Earth's gravity field. Nevertheless, their application to thermosphere studies has resulted in density and wind data sets containing information at unprecedented levels of detail and coverage.

Analyses of accelerometer-derived density data sets resulted in the publication of a large number of scientific papers, on topics including the response to drivers such as solar EUV variability [32, 64], geomagnetic activity and storms [10, 26, 44, 45, 48, 54, 61, 74], substorms [73], Joule heating [75], solar flares [52], solar wind streams [47]; and on phenomena such as the equatorial mass density anomaly [49–51, 58], medium- to large-scale variability [7], upwelling in the cusp region [55, 72], travelling atmospheric disturbances [6, 8], solar terminator waves [27, 53, 62], atmospheric tides [28, 65] and wave structures at solar minimum [9]. These investigations generally made use of density data processed using algorithms published by Bruinsma and Biancale [5], Bruinsma et al. [4], Sutton et al. [74], Sutton et al. [76], Liu et al. [49] and Rentz and Lühr [72].

Investigations of wind results from the CHAMP mission have started to appear in recent years as well. These papers can be classified by their focus on either the equatorial to mid-latitudes [33, 34, 50, 53, 57] or the polar regions [30, 31, 56]. An important early paper on wind derivation from accelerometer data is that by Marcos and Forbes [59] who analysed triaxial accelerometer measurements from the SETA instrument flown on several spacecraft in the early 1980s. Recent publications on the derivation of winds from CHAMP data are provided by Liu et al. [50], Sutton et al. [75].

This section contributes to this research topic by presenting an improved, more generally applicable iterative density and wind derivation algorithm, recently published by Doornbos et al. [18]. The basic problem to be solved by such an algorithm is that the accelerometer delivers at most three orthogonal acceleration observations. However, there are at least four unknowns: Density and three orthogonal wind velocity components. The solution to this problem lies in the fact that the orbital velocity of the satellite is much greater than the wind velocity. The error in the total relative velocity, and therefore in the density, can be kept limited by assuming that the in-track wind speed is zero, or by applying an in-track wind value from an empirical model. Eliminating this unknown from the equation enables the determination of reasonably accurate density values, as well as wind speed components orthogonal to the in-track direction.

4.2.1 Accelerations and Velocities

Figure 4.4 provides a simple schematic view of the three vectors of importance for a density and wind retrieval algorithm: The observed and modelled aerodynamic accelerations $\boldsymbol{a}_{\mathrm{obs}}$ and $\boldsymbol{a}_{\mathrm{mod}}$ are shown originating in the centre of mass of the satellite. In addition, the relative velocity $\boldsymbol{v}_{\mathrm{r}}$ of the atmosphere with respect to the spacecraft

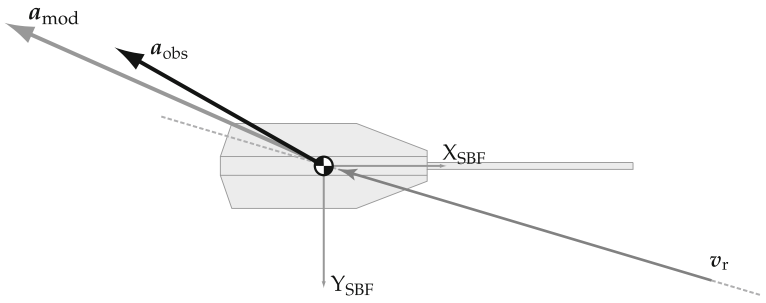

Fig. 4.4 Relative velocity, modelled and observed accelerations in the CHAMP spacecraft body-fixed (SBF) XY plane. CHAMP is viewed from the top

is shown. This quantity is partly observed and partly modelled, as will be explained below. Note that due to the asymmetrical shape of the satellite with respect to the flow, the acceleration is in general not exactly aligned with the relative velocity, as indicated by the dashed guide lines.

The modelled and observed aerodynamic acceleration vectors initially do not match in magnitude and direction. This is mainly due to the approximate character of the modelled density and wind speed. It is the purpose of the new algorithm to find those density and wind values, which, when replacing the original values, make these accelerations match.

Before more detailed descriptions of the previous and new algorithms are provided, the relationship between the parameters in Fig. 4.4 and the way in which they can be obtained from satellite observation data sets and models will be described. The description in the following sections will refer to the instruments and data products of the current generation of accelerometer missions (CHAMP and GRACE) and to the external models (atmospheric models, force models, etc.) that are currently available. The new algorithm is not limited by the use of these data sets and models, however. It can be applied just as well to equivalent data from historical or future accelerometer missions and using future improvements to external models.

Relative Velocity

The relative velocity of the atmosphere with respect to the spacecraft was described in Sect. 3.2.1 as the sum of contributions from the inertial velocity of the spacecraft in its orbit, the velocity caused by the corotating atmosphere, and the velocity of winds, with respect to an Earth-fixed atmosphere. For the accelerometer satellites, these can be expressed in satellite body-fixed (SBF) coordinates, as

$$\boldsymbol{v}_{\rm r} = -R_{\rm ib}\boldsymbol{v} + R_{\rm ib}(\boldsymbol{\omega}_{\oplus} \times \boldsymbol{r}) + R_{\rm ib}R_{\rm ei}R_{\rm le}\boldsymbol{v}_{\rm w}, \tag{4.8}$$

in which the rotation matrix $R_{\rm ib}$ from the inertial to the satellite body-fixed frame is obtained from star camera observations; the inertial satellite position and velocity,

$\boldsymbol{r}$ and $\boldsymbol{v}$, are obtained by precise orbit determination using tracking observations from the satellite's GPS receiver; $\boldsymbol{\omega}_{\oplus}$ is the Earth's angular velocity vector. The wind velocity $\boldsymbol{v}_{\mathrm{w}}$ is usually specified in local coordinates (East, North, Vertical). The transformation to satellite body-fixed coordinates requires the additional rotation matrices R_{le} from local to the Earth-fixed cartesian coordinate system, based on the satellite's latitude and longitude [63], and the rotation matrix R_{ei} from Earth-fixed to inertial coordinates, based on Earth orientation parameters [60]. The first two contributors to $\boldsymbol{v}_{\mathrm{r}}$, the orbit and corotation velocities, are known at a much higher accuracy than the wind velocity. If model values for $\boldsymbol{v}_{\mathrm{w}}$ are required, these can be obtained from a wind model, such as [19].

In the description of the density and wind retrieval algorithms, we will use the notation $\boldsymbol{v}_{\mathrm{r},0}$ or $\boldsymbol{v}_{\mathrm{r},i=0}$ to indicate an initial guess of the relative velocity, by either neglecting winds or using a wind model. The notation $\boldsymbol{v}_{\mathrm{r},i}$ will designate a relative velocity which already includes an accelerometer-derived wind component.

Observed Aerodynamic Acceleration

The observed aerodynamic acceleration $\boldsymbol{a}_{\mathrm{obs}}$ is obtained from the raw accelerometer data after calibration and removal of non-aerodynamic acceleration signals. Details on the accelerometer instruments of CHAMP and GRACE, their performance and processing of raw data can be found in Touboul et al. [79]. The data is delivered to science users in the form of Level 2 products for CHAMP [29] and Level 1B products for GRACE [11].

Calibration is performed by multiplying the acceleration vector with a 3 × 3 diagonal scale factor matrix, and adding a bias vector:

$$\boldsymbol{a}_{\mathrm{cal}} = S\boldsymbol{a}_{\mathrm{raw}} + \boldsymbol{a}_{\mathrm{bias}} \tag{4.9}$$

The scale factors can often be considered nearly constant [78], while the bias is known to vary on timescales of days and more, under the influence of ageing effects and temperature variations. Changes to the satellite software or switches between the redundant on-board electronics parts can cause abrupt changes in the calibration parameters. The determination of the calibration parameters used in this study for the in-track accelerometer observations is described by Van Helleputte et al. [35], who made use of GPS observations. This method was found to be not sufficiently accurate for the cross-track accelerometer observations, for which an alternative method was applied, as discussed at the end of Sect. 4.2.4.

Various non-aerodynamic signals should be removed from the accelerometer data, including accelerations due to activity of cold gas thrusters for attitude control. If a set of two opposing thrusters is not perfectly balanced, as is often the case, they introduce a residual signal in the linear acceleration, besides the intended angular acceleration. Data around the activation times of these thrusters should therefore be removed. A less obvious example of accelerations that should be removed from the data are those due to mechanical forces caused by electrical current changes on the satellite [25].

Finally, modelled accelerations due to radiation pressure from the Sun $\boldsymbol{a}_{\mathrm{srp}}$, Earth albedo $\boldsymbol{a}_{\mathrm{alb}}$ and Earth infrared radiation $\boldsymbol{a}_{\mathrm{IR}}$ are computed and removed from the calibrated and edited accelerometer data $\boldsymbol{a}_{\mathrm{cal}}$, to arrive at the observed aerodynamic acceleration vector $\boldsymbol{a}_{\mathrm{obs}}$.

$$\boldsymbol{a}_{\mathrm{obs}} = \boldsymbol{a}_{\mathrm{cal}} - \boldsymbol{a}_{\mathrm{srp}} - \boldsymbol{a}_{\mathrm{alb}} - \boldsymbol{a}_{\mathrm{IR}} \tag{4.10}$$

Modelled Aerodynamic Acceleration

The modelled aerodynamic acceleration vector $\boldsymbol{a}_{\mathrm{mod}}$ was extensively discussed in the previous chapter. For the derivation of density and winds, the full vector form of Eq. 3.8 is used.

$$\boldsymbol{a}_{\mathrm{mod}} = \boldsymbol{C}_{\mathrm{a}} \frac{A_{\mathrm{ref}}}{m} \frac{1}{2} \rho v_{\mathrm{r}}^{2} \tag{4.11}$$

The mass m can be obtained by subtracting from the satellite launch mass the amount of cold gas used, which is logged in the satellite's housekeeping data, and made available as a data product.

4.2.2 Direct and Iterative Processing Algorithms

Direct Algorithms for CHAMP and GRACE

Previously published algorithms made use of assumptions about the orientation of the accelerometer in space. For CHAMP and GRACE, the accelerometer instruments are carefully mounted near the satellite centre of mass, with an orientation so that their three axes can be considered perfectly aligned with the spacecraft body-fixed (SBF) axes. The spacecraft are under active attitude control, which keeps these axes within a few degrees of the orbit-fixed along-track, cross-track and radial directions (see Fig. 4.5). The relative orientation of these axes can be expressed in roll, pitch and yaw Euler angles.

Because these Euler angles are relatively small, the inertial orbital velocity of the satellite is kept closely aligned with the $\mathrm{X}_{\mathrm{SBF}}$ axis. In Sect. 3.3, it was shown that accelerations in the velocity direction are the most effective in changing the orbital energy, and therefore have a much larger effect on the orbit than accelerations of similar magnitude in perpendicular directions. This means that the $\mathrm{X}_{\mathrm{SBF}}$ axis of the accelerometer can be more accurately calibrated using positioning data from the GPS instrument [35] than the $\mathrm{Y}_{\mathrm{SBF}}$ and $\mathrm{Z}_{\mathrm{SBF}}$ axes, even without taking into account the larger measured signal. This consideration leads to an approach for density determination [4, 5, 76] where only the projection of the aerodynamic acceleration on the $\mathrm{X}_{\mathrm{SBF}}$ axis is used, as shown schematically in Fig. 4.6. The density can then be solved directly from the X-component of the vector Eq. 4.11:

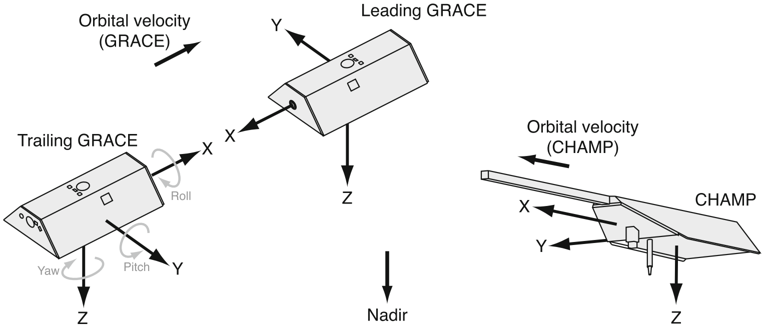

Fig. 4.5 Definition of spacecraft body-fixed (SBF) axes for GRACE and CHAMP. The nadir and velocity directions are shown for the satellite's nominal attitude

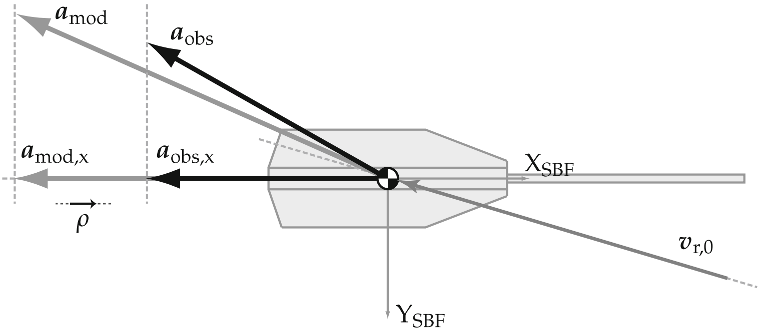

Fig. 4.6 Schematic representation of the determination of density from the projection of acceleration on the X_{SBF} axis

$$\rho = \frac{2m}{A_{\text{ref}} v_{\text{r},0}^2} \frac{a_{\text{obs,x}}}{C_{\text{a,x}}} \tag{4.12}$$

Information from the acceleration component in the Y_{SBF} direction, closely aligned with the cross-track direction, can be used to derive data on the wind speed in that direction. Sutton et al. [76] describe two approaches. In the first approach, $\boldsymbol{C}_{\text{a}}$ in Eq. 4.11 is expanded using the analytical equations for a panel model, using equations equivalent to (3.62). The resulting expansion is quadratic with respect to $v_{\text{w,y}}$, which can then be solved, resulting in an expression depending on $a_{\text{obs,y}}$ and ρ. Sutton names this approach the single axis method, even though information from both the X- and Y-axes is required, if ρ is to be substituted from Eq. 4.12.

The second approach is named the dual-axis method by Sutton et al. [76], and can be found in an earlier paper by Liu et al. [50] as well. The method requires that the lift and sideways forces are negligible, or are modelled and removed from the acceleration beforehand, so that only the observed acceleration due to drag $\boldsymbol{a}_{\text{obs,D}}$ remains. The authors do not specify exactly how the lift and sideways forces should

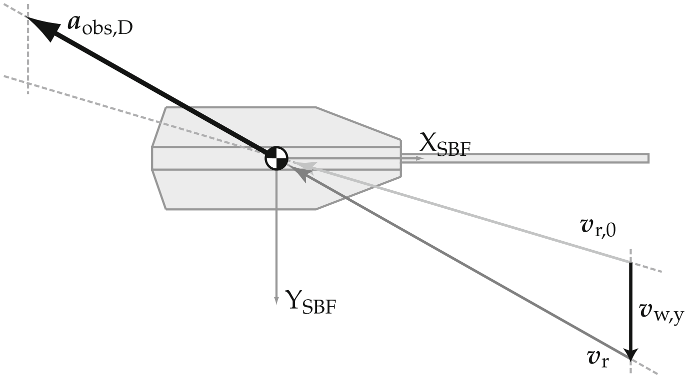

Fig. 4.7 Schematic representation of the determination of wind from the accelerometer Y_{SBF} axis

be modelled, but we have adopted the following approach: first, a new modelled aerodynamic acceleration is computed according to Eq. 4.11, now with the density from Eq. 4.12 and with the a-priori relative velocity $\boldsymbol{v}_{\mathrm{r,0}}$ as inputs. This acceleration vector $\boldsymbol{a}_{\mathrm{mod}}$ can then be decomposed into a drag component, by projection on the relative velocity direction, and a perpendicular lift plus sideways force component, by subtraction of that drag component from the original modelled acceleration. In equations:

$$\boldsymbol{a}_{\mathrm{mod,D}} = (\boldsymbol{a}_{\mathrm{mod}} \cdot \hat{\boldsymbol{v}}_{\mathrm{r,0}})\hat{\boldsymbol{v}}_{\mathrm{r,0}}, \quad \boldsymbol{a}_{\mathrm{mod,L}} = \boldsymbol{a}_{\mathrm{mod}} - \boldsymbol{a}_{\mathrm{mod,D}} \tag{4.13}$$

The modelled lift plus sideways aerodynamic force $\boldsymbol{a}_{\mathrm{mod,L}}$ is then subtracted from the observed aerodynamic acceleration, to arrive at the observed drag.

$$\boldsymbol{a}_{\mathrm{obs,D}} = \boldsymbol{a}_{\mathrm{obs}} - \boldsymbol{a}_{\mathrm{mod,L}} \tag{4.14}$$

The velocity and drag acceleration are by definition in the same direction, so that the wind can be determined from a simple geometrical consideration (see Fig. 4.7). Expressed in the form of an equation, ρ and $\boldsymbol{C}_{\mathrm{D}}$ disappear when the Y-component of Eq. 3.10 is divided by the X-component, and $v_{\mathrm{w,y}}$ is solved for after substitution of Eq. 4.8, resulting in:

$$v_{\mathrm{w,y}} = \frac{a_{\mathrm{obs,D,y}}}{a_{\mathrm{obs,D,x}}} v_{\mathrm{r,0,x}} - v_{\mathrm{r,0,y}} \tag{4.15}$$

A similar wind determination could in principle be performed for the Z_{SBF} axis. However, the aerodynamic acceleration in this direction is in general too small compared to errors in the instrument calibration, radiation pressure model and lift force model. In addition, on the CHAMP accelerometer, this Z_{SBF} component suffers from a malfunction which prevents the acquisition of accurate data [68].

Discussion of the Direct Algorithms

The schematic representations in Figs. 4.6 and 4.7 clearly show that when the angle between the relative velocity and the $\mathrm{X}_{\mathrm{SBF}}$ axis gets larger, the errors in the density and wind increases. For the extreme case where this angle approaches 90 degrees, density values will approach zero, while the wind speed will go to infinity. In these figures, the angles are exaggerated for clarity, compared to the angles of CHAMP and GRACE under nominal attitude control. The roll, pitch and yaw Euler angles are kept within ±1 degree for GRACE and ±2 degrees for CHAMP. For the future Swarm mission, the attitude will likely be somewhat more loosely controlled, probably to within ±4 degrees.

These attitude angles only determine the alignment of the body-fixed frame with the inertial velocity vector. The contributions to the relative velocity vector by the co-rotation of the atmosphere and thermosphere winds can be equally important. The atmospheric co-rotation velocity over the equator depends on the altitude, ranging from 483–502 m/s at 250–500 km. This increases the maximum angle between the relative velocity and the X_{SBF} axis by 3.6–3.8 degrees. The wind speed, which under most conditions is within the range of about 0–200 m/s, can reach peak velocities in the polar regions of up to 500–1,000 m/s [56, 30], causing the incidence angle to reach peak values of 8–10 degrees. In principle, the accuracy of the derived density and wind speed should be independent of these angles, but when using the direct approach this is not the case.

Another limiting factor of the direct algorithm results from the dependence of $\boldsymbol{C}_{\mathrm{a}}$ on $\boldsymbol{v}_{\mathrm{r}}$. The methods use an initial value $\boldsymbol{v}_{\mathrm{r},0}$, composed of the orbit and co-rotation velocity, and either neglect or model the in-track wind velocity. After the derivation of the cross-track wind $v_{\mathrm{w,y}}$ however, there is a better estimate of the relative velocity:

$$\boldsymbol{v}_{\mathrm{r},i=1} = \boldsymbol{v}_{\mathrm{r},0} + \boldsymbol{v}_{\mathrm{w,y}} \tag{4.16}$$

where the index i is an iteration counter. This new relative velocity leads to a new value of $\boldsymbol{C}_{\mathrm{a}}$ (according to the equations in the previous chapter) and therefore to a new value of ρ. The change in $\boldsymbol{C}_{\mathrm{a}}$ also leads to a change in the lift and sideways components of the aerodynamic acceleration, which are to be removed from $\boldsymbol{a}_{\mathrm{obs}}$ to arrive at $\boldsymbol{a}_{\mathrm{obs,D}}$, yielding a new value for $v_{\mathrm{w,y}}$. This chain of dependencies indicates that an iterative algorithm could be required to determine the density and wind speed with the highest possible accuracy.

Iterative Algorithm

This section presents an iterative algorithm, which avoids the restrictions and sources of error discussed in the previous section. Figure 4.8 illustrates schematically the principle of the algorithm in two steps. The goal of the algorithm is to make the modelled aerodynamic acceleration $\boldsymbol{a}_{\mathrm{mod}}$ match the direction (top panel) and subse-

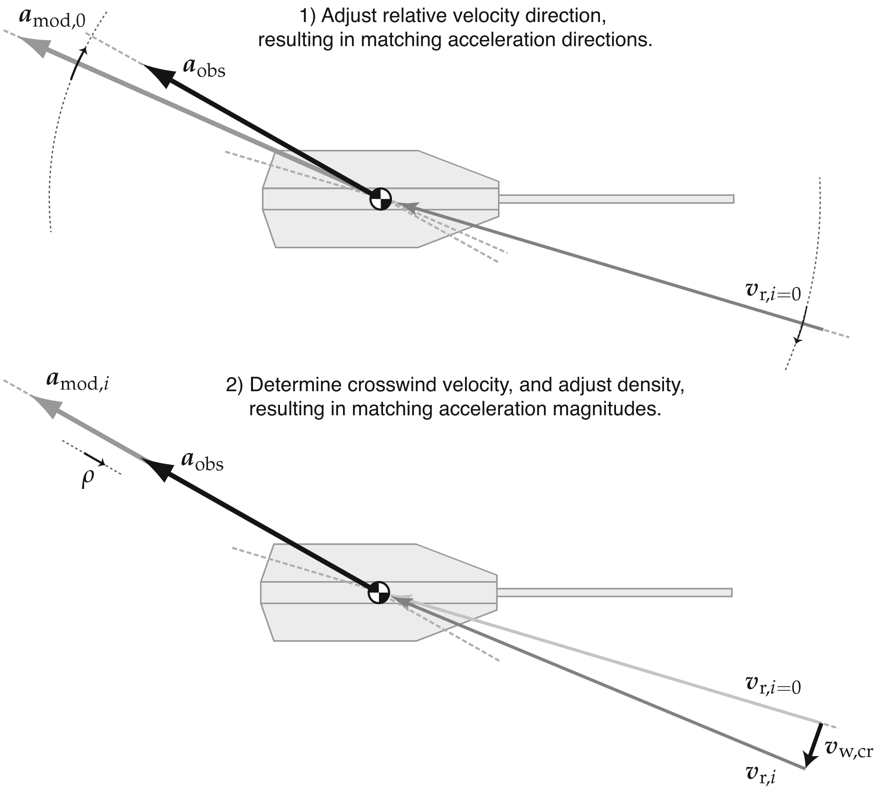

Fig. 4.8 Schematic overview of the iterative wind and density derivation algorithm for accelerometer satellites

quently the magnitude (bottom panel) of the aerodynamic acceleration observed by the accelerometer $\boldsymbol{a}_{\mathrm{obs}}$. This is achieved by first modifying the direction of the relative velocity vector $\boldsymbol{v}_{\mathrm{r}}$, without modifying its magnitude, until the modelled acceleration direction matches that of the observed acceleration. Subsequently the density ρ is modified, so that the magnitude of the accelerations matches.

The adjustment to the orientation is made by a rotation of the relative velocity about the local vertical direction, indicated by the unit vector $\hat{\boldsymbol{u}}_{\mathrm{up}}$. The acceleration components projected on this direction will be set to zero. To simplify the notation, a prime is added to indicate this modification of the acceleration vectors, which is applied repeatedly:

$$\boldsymbol{a}' = \boldsymbol{a} - (\boldsymbol{a} \cdot \hat{\boldsymbol{u}}_{\mathrm{up}})\hat{\boldsymbol{u}}_{\mathrm{up}} \tag{4.17}$$

We will use the sum of the orbital and co-rotation velocities as our a-priori relative velocity:

$$\boldsymbol{v}_{\mathrm{r},i=0} = \boldsymbol{v}_{\mathrm{o}} + \boldsymbol{v}_{\mathrm{c}} \tag{4.18}$$

The possibility of including modelled in-track and vertical wind velocities in the algorithm computation will be discussed at the end of this section.

While modifying the direction of the velocity and modelled acceleration vectors, the magnitude of the acceleration is not of importance. We therefore make use of the unit vectors $\hat{\boldsymbol{a}}'_{\text{obs}}$ and $\hat{\boldsymbol{a}}'_{\text{mod}}$, and according to Eq. 4.11 substitute $\hat{\boldsymbol{C}}_{\text{a}}$ for the latter. We can now define our measure of the acceleration direction residual:

$$\boldsymbol{d} = \hat{\boldsymbol{a}}'_{\text{obs}} - \hat{\boldsymbol{a}}'_{\text{mod},i} = \hat{\boldsymbol{a}}'_{\text{obs}} - \hat{\boldsymbol{C}}'_{\text{a},i}(\boldsymbol{v}_{\mathbf{r},\boldsymbol{i}}, \ldots) \tag{4.19}$$

In practice, if the magnitude of $\boldsymbol{d}$ is below a certain predefined threshold ϵ, convergence has been reached. Otherwise, another iteration is required. The convergence criterion is thus:

$$||\boldsymbol{d}|| < \epsilon \tag{4.20}$$

The unit vector representing the direction of the velocity adjustment for the current iteration is defined to be perpendicular to both the relative velocity and the rotation axis:

$$\hat{\boldsymbol{v}}_{\text{adj},i} = \frac{\boldsymbol{v}_{\text{r},i} \times \hat{\boldsymbol{u}}_{\text{up}}}{||\boldsymbol{v}_{\text{r},i} \times \hat{\boldsymbol{u}}_{\text{up}}||} \tag{4.21}$$

Next, to start our numerical differentiation, two relative velocity vectors are formed, which keep the magnitude of the unadjusted relative velocity, but which are rotated slightly in both directions with respect to the relative velocity of the current iteration:

$$\boldsymbol{v}_{\text{r}}^{+} = ||\boldsymbol{v}_{\text{r},i}||\frac{\boldsymbol{v}_{\text{r},i} + \delta\hat{\boldsymbol{v}}_{\text{adj},i}}{||\boldsymbol{v}_{\text{r},i} + \delta\hat{\boldsymbol{v}}_{\text{adj},i}||}, \quad \boldsymbol{v}_{\text{r}}^{-} = ||\boldsymbol{v}_{\text{r},i}||\frac{\boldsymbol{v}_{\text{r},i} - \delta\hat{\boldsymbol{v}}_{\text{adj},i}}{||\boldsymbol{v}_{\text{r},i} - \delta\hat{\boldsymbol{v}}_{\text{adj},i}||} \tag{4.22}$$

These modified relative velocities will result in modified modelled acceleration directions according to the equations in Chap. 3. The result from both rotation directions is substituted into Eq. 4.19:

$$\boldsymbol{d}^{+} = \hat{\boldsymbol{a}}_{\text{obs}} - \hat{\boldsymbol{C}}'_{\text{a}}(\boldsymbol{v}_{\text{r}}^{+}, \ldots), \quad \boldsymbol{d}^{-} = \hat{\boldsymbol{a}}_{\text{obs}} - \hat{\boldsymbol{C}}'_{\text{a}}(\boldsymbol{v}_{\text{r}}^{-}, \ldots) \tag{4.23}$$

The vector difference between the two velocity vectors is:

$$\Delta\boldsymbol{v}_{\text{r}} = \boldsymbol{v}_{\text{r}}^{+} - \boldsymbol{v}_{\text{r}}^{-}, \tag{4.24}$$

and the effect of this velocity rotation on the acceleration direction residual is:

$$\Delta d = ||\boldsymbol{d}^{+}|| - ||\boldsymbol{d}^{-}|| \tag{4.25}$$

Now, all the elements are in place to compute the next iteration of the relative velocity, which keeps the magnitude of the original velocity, but changes the direction.

$$\boldsymbol{v}_{\mathrm{r},i+1} = ||\boldsymbol{v}_{\mathrm{r},i}|| \frac{\boldsymbol{v}_{\mathrm{r},i} - d(\Delta \boldsymbol{v}_{\mathrm{r}} / \Delta d)}{||\boldsymbol{v}_{\mathrm{r},i} - d(\Delta \boldsymbol{v}_{\mathrm{r}} / \Delta d)||} \tag{4.26}$$

At this point Eqs. 4.19 and 4.20 are reevaluated. If the convergence criterion of Eq. 4.20 is met, we can proceed computing the crosswind speed and mass density.

$$\boldsymbol{v}_{\mathrm{w,cr}} = \boldsymbol{v}_{\mathrm{r},i} - \boldsymbol{v}_{\mathrm{r},i=0} \tag{4.27}$$

$$\rho = \frac{2m}{A_{\mathrm{ref}} v_{\mathrm{r},i}^2} \frac{||\boldsymbol{a}'_{\mathrm{obs}}||}{||\boldsymbol{C}'_{\mathrm{a},i}||} \tag{4.28}$$

Modelling of in-Track and Vertical Winds

In the description of the algorithms above, we have not discussed the possible effect on the aerodynamics of wind components other than the cross-track component. Since we are interested in retrieving the crosswind $\boldsymbol{v}_{\mathrm{w,cr}}$ from the accelerometer data, a model value for this component should not be included in the a-priori relative velocity of Eq. 4.18. A model value for the in-track wind $\boldsymbol{v}_{\mathrm{w,it}}$, and the wind in the direction of the rotation axis $\boldsymbol{v}_{\mathrm{w,z}}$ could be applied in that equation however. These can be computed by projecting the full model wind on the unit vectors in these directions.

$$\boldsymbol{v}_{\mathrm{w,it}} = (\boldsymbol{v}_{\mathrm{w,mod}} \cdot \hat{\boldsymbol{v}}_{\mathrm{r}})\hat{\boldsymbol{v}}_{\mathrm{r}} \tag{4.29}$$

$$\boldsymbol{v}_{\mathrm{w,up}} = (\boldsymbol{v}_{\mathrm{w,mod}} \cdot \hat{\boldsymbol{u}}_{\mathrm{up}})\hat{\boldsymbol{u}}_{\mathrm{up}} \tag{4.30}$$

Since $\hat{\boldsymbol{v}}_{\mathrm{r}}$ changes its direction during the iterative process described in the previous section, Eq. 4.29 will have to be reevaluated and $\boldsymbol{v}_{\mathrm{r}}$ in Eqs. 4.22 and 4.26 will have to be updated after each iteration step.

The influence of the use of a model for the in-track wind on the density and crosswind data will be evaluated in Sect. 4.2.4

4.2.3 *Example of CHAMP* and *GRACE density and wind processing*

Figures 4.9 and 4.10 show examples of the inputs and outputs of the density and wind processing algorithms for two orbits of CHAMP and GRACE. The selected orbits are on April 5, 2005, when the two satellites were in nearly the same orbital plane, with local solar times of ascending and descending equator crossings at approximately 12:50 and 00:50, respectively. The time span for the GRACE data in Fig. 4.10 is shifted forward by 20 min with respect to the one for CHAMP in Fig. 4.9, so that the series for both satellites start near the ascending node. A geomagnetic storm

($K_p = 7$) occurred a few hours before the orbits that are shown here. CHAMP was at an approximate mean altitude of 360 km, while GRACE was at 470 km.

Velocity Inputs

Concentrating on the velocities first, it is clear that the X-direction for both spacecraft is dominated by the nearly constant orbital velocity. The velocities in the Y- and Z-directions are an order of magnitude smaller. In the Y-direction, the sinusoidal pattern of the velocity due to the corotating atmosphere is clearly visible, although the wind model and projection of the orbital velocity on this axis also show clear contributions. In the Z-direction, the projections of the corotation and horizontal wind are nearly zero. The orbital velocity projected on the Z-axis still results in a signal of up to about 100 m/s though. The behaviour of this component is determined by the satellite's pitch rotations. For CHAMP, the attitude thruster actuations are clearly visible as changes in slope. For GRACE, the pitch motion is controlled to keep accurate pointing between the twin satellites, resulting in a sinusoidal variation at the orbital period.

Acceleration Inputs

The top-right frames of Figs. 4.9 and 4.10 show both the observed and modelled accelerations. Note that observed accelerations in the Z-direction for CHAMP are missing from Fig. 4.9 though, because of a malfunction in the instrument.

The aerodynamic accelerations are dominant in the X-direction for both satellites, while in the Y-direction, this is true for CHAMP but not for GRACE. This is because the magnitude of the aerodynamic acceleration for GRACE is about one fifth of that of CHAMP, but the radiation pressure is about the same for both satellites.

Note that the modelled radiation pressure and total observed accelerations contain jumps at eclipse entries and exits. These jumps can be used to check the accuracy of the radiation pressure model and calibration scale factor. The observed aerodynamic acceleration, which is computed by taking the difference between these two, should not show such jumps, if eclipses are correctly modelled and the scale factors used in the accelerometer calibration are determined correctly.

Density Results

The density and crosswind results from both the direct and iterative algorithm are shown at the bottom of Figs. 4.9 and 4.10.

The density results for the direct and iterative algorithms are nearly identical. This indicates that the assumption of the direct algorithm that the accelerometer X-axis is closely aligned with the along-track axis is valid for the purpose of density determination. Despite the altitude difference of 110 km, the retrieved densities for

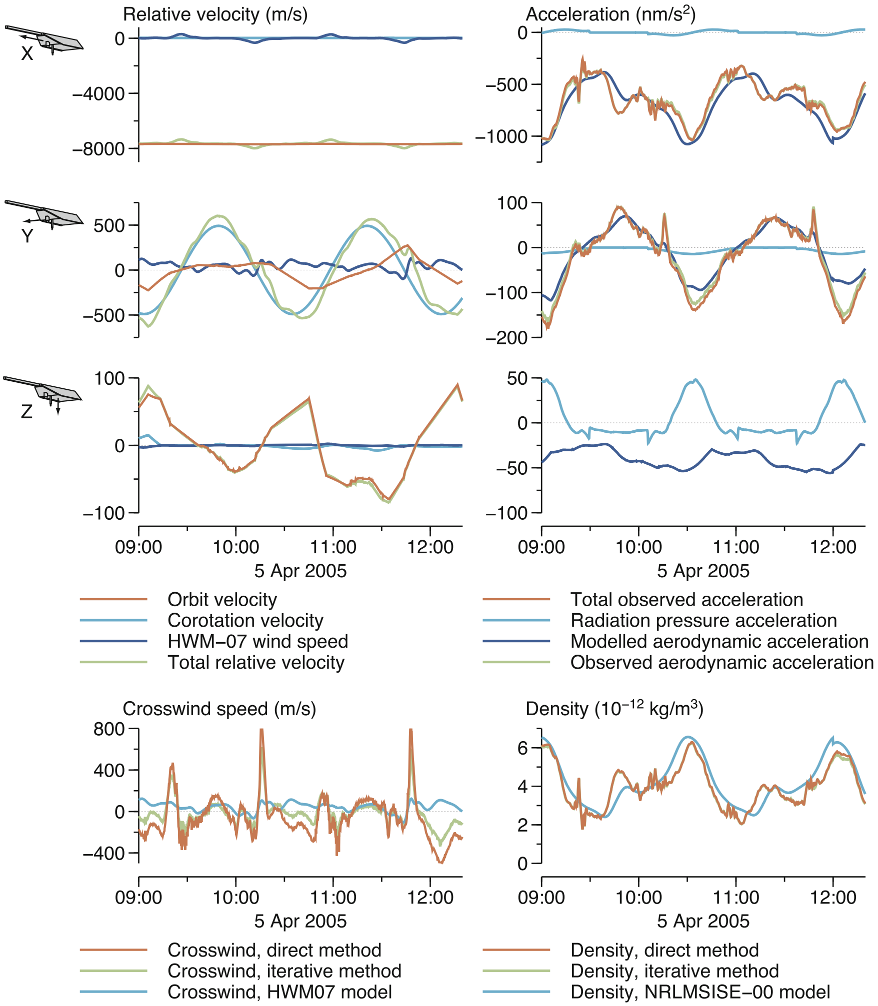

Fig. 4.9 Time series of relative velocity components (*left*) and acceleration components (*right*) in the body-fixed frame for CHAMP

the two satellites show many similar variations. The high-frequency variations in the data, which are not present in the NRLMSISE- 00 model, should be especially interesting for interpretation. A closer look at this data, and that of the surrounding days, will be provided in Chap. 5.

Crosswind Results

Note how for both satellites the crosswind pattern is quite different than that predicted by the HWM07 model. Especially the peak winds, encountered when crossing the

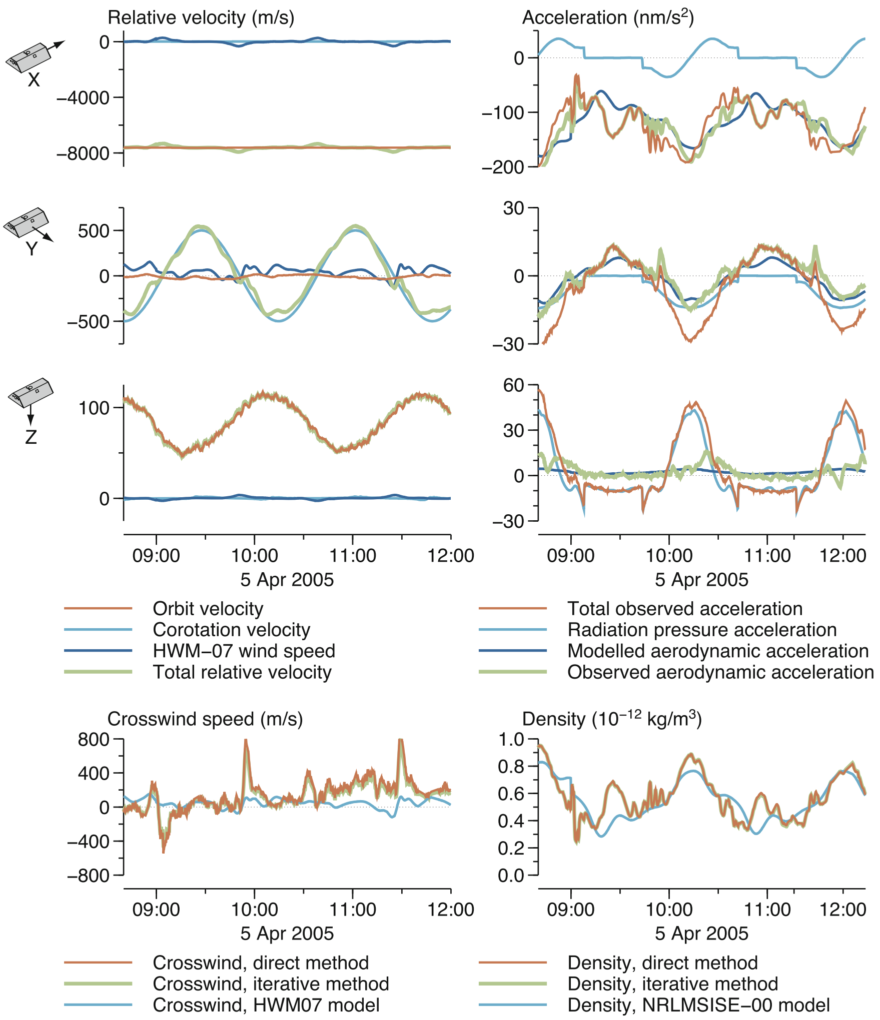

Fig. 4.10 Time series of relative velocity components (*left*) and acceleration components (*right*) in the body-fixed frame for GRACE-B

auroral zones, are much larger (up to 600 m/s). This discrepancy, which is certainly not specific to the two orbits shown here, will be further discussed in Chap. 5 as well.

The direct algorithm winds are, in general, even larger than those from the iterative algorithm. This difference is larger for CHAMP than for GRACE. This can be explained by the wider attitude deadband for CHAMP. This adversely influences the close alignment between spacecraft axes and orbit axes, which is required for the accuracy of the direct algorithm. The smaller crosswind outcome of the iterative algorithm is thought to be the more accurate.

The crosswind time series for GRACE shows a positive slope. This is most likely the result of a positive trend in the accelerometer Y-axis bias, which was not taken into account in the calibration.

Before proceeding with further interpretations of the density and wind output data in Chap. 5, the accuracy of the direct and iterative algorithm results, and their sensitivity to error sources, is evaluated using simulated data in the next section. Such an evaluation provides important insights into the reliability of the results.

4.2.4 Error Assessment Using Simulated Accelerometer Data

Simulated aerodynamic acceleration data were generated by applying Eq. 4.11, using modelled density ρ_m and wind $\boldsymbol{v}_\mathrm{w,m}$ values from the NRLMSISE-00 density model [69] and the HWM07 wind model [19]. Real CHAMP attitude and orbit data were used both in the generation of these simulated acceleration data and in the application of the retrieval algorithms. The accuracy of the algorithm results, comprising the density ρ and crosswind $v_\mathrm{w,y}$ or $v_\mathrm{w,cr}$ can then be tested by examining density and wind residuals r_ρ and r_v.

The density residuals are expressed as percentages, relative to the simulated density signal:

$$r_\rho = \frac{\rho - \rho_\mathrm{m}}{\rho_\mathrm{m}} \cdot 100\% \tag{4.31}$$

The wind residuals are defined as the differences between the retrieved wind speed and the modelled wind speed's projection on the direction of the retrieved wind speed:

$$r_v = v_\mathrm{w,y} - \boldsymbol{v}_\mathrm{w,m} \cdot \hat{\boldsymbol{v}}_\mathrm{w,y} \quad \text{or} \quad r_v = v_\mathrm{w,cr} - \boldsymbol{v}_\mathrm{w,m} \cdot \hat{\boldsymbol{v}}_\mathrm{w,cr} \tag{4.32}$$

Six cases for simulated errors are defined. In the first case, labeled "Identical input", the exact same models and input data were used in the retrieval algorithm that had been originally applied in the creation of the simulated accelerations. This allows for an assessment of the errors that are purely inherent in the algorithm.

However, it is also important to evaluate the algorithms under the influence of the uncertainties in the input data and models. In two further cases, named "$\mathrm{X_{SBF}}$ offset" and "$\mathrm{Y_{SBF}}$ offset", a value of 10 $\mathrm{nm/s^2}$ was added to the simulated acceleration data in either direction, before applying the algorithms. For each single measurement, such an offset could be the result of an error in the instrument calibration, or due to errors in the removal of radiation pressure and attitude thruster accelerations. The magnitude of 10 $\mathrm{nm/s^2}$ was found to be typical for the order of magnitude of such errors. However, each of these error sources comes with its own temporal variation of the acceleration error, and their effects can either add up or (partly) cancel each other out over time. Therefore, the constant 10 $\mathrm{nm/s^2}$ offset introduced here should be viewed as just a crude approximation, which should nevertheless give some idea of the sensitivity of the density and wind derivation algorithms. In the fourth test case, named “In-track wind”, the HWM07 modelled wind in the in-track direction was neglected in the density and crosswind derivation algorithms.

Two further test cases are used to assess the effect of force model errors. The simulated aerodynamic accelerations were generated with a value of $\alpha = 0.93$ for the energy flux accommodation parameter in the aerodynamic model. In the “Energy accommodation” case, this value was changed to $\alpha = 0.88$ for the density and wind retrieval. This 5% difference can be used to represent one aspect of the inherent uncertainty in the gas-surface interaction modelling. The final test case, named “Panel model”, is used to represent the uncertainty in the satellite geometry model for complexly shaped satellites such as CHAMP. Our own adjusted panellised geometrical model of the CHAMP satellite [17] used in the simulated data generation was replaced by an alternative one [5] in the density and wind retrieval. This replacement amounts to a reduction in frontal area of around 14% when the satellite is viewed along the X_{SBF} axis (front), and of 8% when viewed along the Y_{SBF} axis (side).

The statistics of the density retrieval residuals over the complete year 2004 (~ 3.15 million measurements), are presented in Table 4.1. During this year, CHAMP flew only in its nominal attitude mode for which the direct algorithm is applicable. The data in the table shows that the iterative algorithm leads to lower density residuals than the direct approach in the “Identical input” case. With the 10 nm/s^2 Y_{SBF} acceleration offset, this ranking is shifted however, because the iterative algorithm is sensitive to this acceleration component, while the direct algorithm is not. Both algorithms show an equal sensitivity to in-track wind errors. The direct algorithm seems slightly more sensitive to the force-model related errors though, if judged by the standard deviations. Note that for the force model related errors, the mean values are generally larger than the standard deviations, indicating that these accelerometer-derived density data are affected by mostly systematic errors. The data will therefore be more suitable to studies of relative changes in density than for use in modelling approaches which require absolute density values.

In the wind residual statistics, presented in Table 4.2, the advantage of the iterative algorithm over the direct approach is evident, certainly for the “Identical input” case. For both algorithms, the 10 nm/s^2 error introduced in the Y_{SBF} direction of the accelerations has a very large detrimental effect on the accuracy of the crosswind speed, leading to maximum errors of 915 m/s (iterative) and 1,283 m/s (direct). Such very large wind errors will occur in the real data processing when the aerodynamic acceleration signal in the Y_{SBF} direction is small compared to the instrument calibration, instrument noise and radiation pressure errors for that direction. These large wind errors are therefore prevalent at conditions of low density, such as at higher orbital altitudes and lower solar activity levels. For this reason, it is currently not possible to routinely acquire an accurate crosswind derivation from the GRACE satellites, which are at a higher altitude than CHAMP.

An important factor in this respect is the magnitude of cross-track radiation pressure accelerations and related acceleration errors. This magnitude is at a maximum when the satellite’s orbital plane is near-perpendicular to the Sun-Earth vector (dawn-

Table 4.1 Statistics of the density retrieval residuals, in percentages of the density signal

Direct algorithm	Min.	Mean	Max.	RMS	Std.
Identical input	3.3	0.0	5.5	0.7	0.7
X_{SBF} offset	-17.4	-2.7	3.8	3.1	1.5
Y_{SBF} offset	-3.3	0.0	5.5	0.7	0.7
In-track wind	-10.8	0.2	14.3	2.2	2.1
Energy accomm.	-4.8	-1.7	3.7	1.9	0.7
Panel model	3.5	7.8	14.0	7.9	0.9
Iterative algorithm	Min.	Mean	Max.	RMS	std.
Identical input	-0.5	0.0	0.0	0.0	0.0
X_{SBF} offset	-17.4	-2.9	0.5	3.2	1.4
Y_{SBF} offset	-12.3	-0.3	4.5	1.6	1.6
In-track wind	-10.9	0.2	13.6	2.0	2.0
Energy accomm.	-2.1	-1.6	-0.7	1.6	0.2
Panel model	5.7	8.1	9.0	8.1	0.3

Table 4.2 Statistics of the wind retrieval residuals, in m/s

Direct algorithm	Min.	Mean	Max.	RMS	std.
Identical input	-225	-1	202	38	38
X_{SBF} offset	-226	-2	210	44	44
Y_{SBF} offset	-173	209	1,285	236	110
In-track wind	-228	-2	205	38	38
Energy accomm.	-258	-1	222	52	52
Panel model	-262	-2	224	54	54
Iterative algorithm	Min.	Mean	Max.	RMS	Std.
Identical input	-9	-0	10	1	1
X_{SBF} offset	-44	3	81	12	12
Y_{SBF} offset	-242	81	915	140	114
In-track wind	-9	-0	10	1	1
Energy accomm.	-55	-0	51	21	21
Panel model	-52	0	49	22	22

dusk orbit). We have also encountered particularly extreme wind errors around eclipse transitions. A small discrepancy between the modelled and true eclipse geometry will lead to short periods with an incorrect application or removal of the full modelled radiation pressure acceleration, which has a maximum magnitude of around 40 nm/s^2 for CHAMP, leading to wind errors far exceeding 1,000 m/s.

The results in Table 4.2 show that the crosswind derivation is practically insensitive to errors in the in-track wind, since the results are nearly the same as for the "Identical input" case. The other error sources also have only minor effects in comparison to the Y_{SBF} offset.

It should be clear that a large aerodynamic signal strength, a careful calibration of the accelerometer in the crosswind direction and an accurate modelling of cross-track radiation pressure accelerations are a necessity for the derivation of accurate crosswind results.

The Y_{SBF} (cross-track) calibration for the CHAMP and GRACE satellites using GPS data is problematic [35], because of the relatively low acceleration signal, and because of the limited capability of accelerations in this direction to perturb the orbit, compared to along-track accelerations. Both limitations are the result of fundamental orbital dynamics in combination with the tight attitude control of the spacecraft, as discussed in Sect. 3.3 and the start of Sect. 4.2.2, respectively. We therefore adopted an alternative approach to calibrate CHAMP's Y_{SBF} accelerometer data, analogous to Sutton et al. [76]. We took density observations derived using the direct method from the X_{SBF} data, and combined these with the aerodynamic satellite model to arrive at simulated observations for the Y_{SBF} data. The accelerometer data for this direction was then calibrated by estimating the biases that minimize the difference between the data and these simulated observations. We have checked the reliability of these biases by comparing the local time variation of the zonal wind from ascending arcs with those from descending arcs and found no systematic difference. An error in the Y_{SBF} biases would influence the ascending and descending wind profiles in opposite directions.

4.3 Force Model Parameter Estimation From Precise Tracking Data

A third important technique for analysing orbital dynamics in terms of aerodynamics is *Precise orbit determination*, named *special perturbations orbit determination* by the space surveillance community. This approach was already briefly mentioned in Sect. 4.1.3. The technique involves numerically integrating the system of second order differential Eq. 3.5 from an initial position and velocity. Precise force models are applied to integrate the motion of the satellite, in order to obtain estimates of the positions and velocities over a certain time span, the *orbit arc*.

The length of this time span is usually between a few hours and a few days, depending on the temporal density of the tracking data (denser data enable shorter arcs), the quality of the models (better models allow longer arcs), as well as operational constraints.

Due to errors and uncertainties in the initial conditions, force models and measurement models, the initially integrated orbit likely does not fit well with tracking observations. The orbit estimate can then be iteratively improved by least-squares fitting the initial position, velocity and model parameters that result in minimal tracking data residuals. The procedure is explained in great detail by, e.g., Montenbruck and Gill [63] and Tapley et al. [77].

Information on the effect of atmospheric density on the orbit can be recovered in the same process. This involves estimation of carefully selected force model parameters, which will be designated with the letter p in the sections below.

Three parameterisation methods will be briefly described below, even though their results will not be directly analysed in the remainder of this work. The other two methods presented earlier in this chapter are easier to implement and result in a better spatial sampling of the data. Nevertheless, the force model parameter estimation method is important for accelerometer data calibration. It could also be an essential part of future thermosphere density studies, especially at altitudes above about 500 km, where the accuracy of TLE-derived data is insufficient and accelerometers are unavailable.

4.3.1 Estimating Aerodynamic Scale Factor Parameters

In the first parameterisation method, the computed aerodynamic acceleration is multiplied with an aerodynamic scale factor parameter p_a.

$$\ddot{\boldsymbol{r}}_\mathrm{a} = p_\mathrm{a} \boldsymbol{C}_\mathrm{a} \frac{A_\mathrm{ref}}{m} \frac{1}{2} \rho_\mathrm{M} v_\mathrm{r}^2 \tag{4.33}$$

Assuming that errors in the measurements, measurement modelling and force models are negligible, the effect of the true density on the drag force will be close to that of the scale factor times the modelled density over the time span. The mean true density is then approximately equal to

$$\bar{\rho} \approx p_\mathrm{a} \bar{\rho}_\mathrm{M} \tag{4.34}$$

Note that the parameter p_a represents the data over model density ratio for a certain time interval, similar to those discussed in Sect. 2.6.1. The use of these ratios facilitates direct comparisons of the data between different methods and different objects.

Time-Dependent Estimation, Parameter Observability and Correlations

The estimated parameter, such as p_a in the equation above, does not necessarily have to be valid for the entire arc. When longer arcs are used, the force model can be adjusted using a time series of piecewise constant or piecewise linear parameters, each of which is valid for a certain *sub-arc*. The orbit analyst can therefore select the temporal resolution of the model adjustment.

This leads to the related topics of parameter observability and correlations between estimated parameters. In principle, the number of force model parameters that can be estimated is limited by the coverage of tracking observations. For modern techniques, such as GPS and DORIS this number will be very large. As more and more force model parameters are estimated this will almost certainly result in an improved least-squares fit of the orbit with the tracking observations. However, this does not

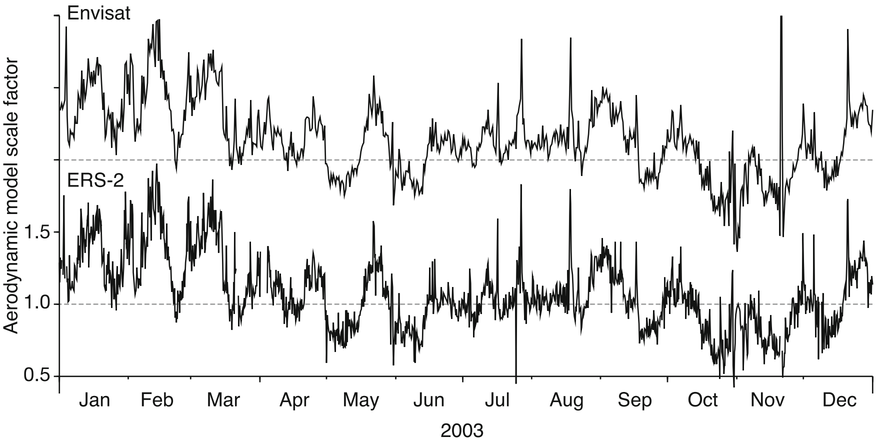

Fig. 4.11 Aerodynamic model scale factors, estimated from tracking data of ERS-2 and Envisat (offset by 1.0)

automatically mean that the estimated parameters are suitable for further processing into data on the thermospheric density and wind.

Over shorter time intervals, there is an increased chance that the parameters are affected by errors in the measurements or other force models, besides the aerodynamics. In addition, estimated parameters could be correlated, which means that adjustment of different parameters has a similar effect on the orbit fit. Solutions to these problems are either to eliminate certain estimation parameters, or constrain their solution to a-priori values. Neither solution is ideal, and interpretations of the results of parameter estimations should always be made while being aware of these possible shortcomings.

Examples of these limitations will be provided when other parameterisation schemes are discussed in the next sections. But first an example will be provided of the results of aerodynamic force model scale factor estimation.

ERS-2 and Envisat Example

Figure 4.11 shows results that were first presented in Doornbos et al. [15]. The time series of p_a shown in the Figure have been estimated for adjacent 6 h intervals, making use of SLR and DORIS tracking data for Envisat and of SLR tracking for ERS- 2. Accurate ANGARA models (see Sect. 3.5) were used to model the geometry and gas-surface interaction for both satellites [13]. NRLMSISE- 00 was used to model the density. Since radiation pressure and gravity forces can be fairly accurately modelled for both satellites, the plotted values mainly represent NRLMSISE- 00 density modelling errors, corresponding to Eq. 4.34.

The time series for ERS- 2 and Envisat are nearly identical, due to their similar orbits, which are near-circular with frozen eccentricity, sun-synchronous, near-polar and at an altitude of approximately 800 km. The only difference between the orbits is the right-ascension of the ascending node. ERS- 2 crosses the equator at 10:30/22:30 local solar time, while Envisat precedes it by 30 min at 10:00/22:00.

The Envisat time series contains less noise, which is due to the availability of the dense DORIS tracking data, compared to the more sparse SLR data which has been the only source of data that was used for ERS- 2. There are a few peaks distinct to each satellite, which are due to manoeuvres. Orbit arcs containing manoeuvres should therefore be eliminated before further analysis in terms of thermosphere density takes place. There are also some peaks, for instance in July and August, which are common to both ERS- 2 and Envisat. These probably indicate short-term disturbances in the atmosphere, which are not properly represented in the NRLMSISE- 00 density model.

4.3.2 Estimating Empirical Acceleration Parameters

A different estimation approach starts by eliminating the detailed non-gravitational force models altogether in the orbit determination. Instead, empirical accelerations $\ddot{\boldsymbol{r}}_\mathrm{E}$ are estimated directly. At a later time, these accelerations can then be processed much like calibrated accelerometer observations, as described in Sect. 4.2.

A basic parameterisation scheme for this method is to introduce piecewise constant empirical acceleration parameters p in the three orthogonal orbit-fixed directions, where the subscripts A, C and N signify the along-track, cross-track and in-plane normal directions, respectively (see Fig. 3.4).

$$\ddot{\boldsymbol{r}}_\mathrm{a} \approx p_\mathrm{A}\hat{\boldsymbol{u}}_\mathrm{A} + p_\mathrm{C}\hat{\boldsymbol{u}}_\mathrm{C} + p_\mathrm{N}\hat{\boldsymbol{u}}_\mathrm{N} \tag{4.35}$$

Note however, that both in-plane acceleration components affect the shape of the orbit (see Sect. 3.3). These accelerations can therefore not easily be distinguished using tracking observations. The parameters p_A and p_N are therefore correlated. Usually, only the along-track component is estimated, since both its magnitude and effect on the orbit are generally much larger than the radial component. The radial acceleration in Eq. 4.35 is then set to zero.

The same caveat applies to a more elaborate 9-parameter estimation, which includes harmonic variations of the empirical acceleration as a function of the argument of latitude ν.

$$\begin{aligned}\ddot{\boldsymbol{r}}_\mathrm{a} \approx\ & (p_\mathrm{A} + p_\mathrm{A,c}\cos(\nu) + p_\mathrm{A,s}\sin(\nu))\hat{\boldsymbol{u}}_\mathrm{A} \\ & + (p_\mathrm{C} + p_\mathrm{C,c}\cos(\nu) + p_\mathrm{C,s}\sin(\nu))\hat{\boldsymbol{u}}_\mathrm{C} \\ & + (p_\mathrm{N} + p_\mathrm{N,c}\cos(\nu) + p_\mathrm{N,s}\sin(\nu))\hat{\boldsymbol{u}}_\mathrm{N}\end{aligned} \tag{4.36}$$

These harmonic accelerations are resonant at the orbital period and are therefore effective at changing the orbital elements (see Sect. 3.3). This has proved to be a

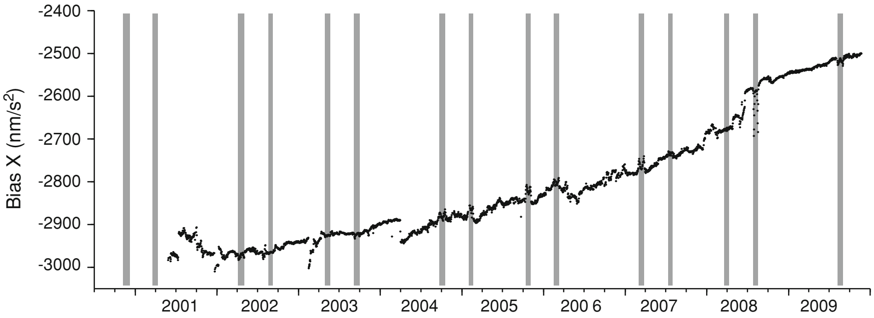

Fig. 4.12 Biases in the X-component of the CHAMP accelerometer data, estimated using GPS tracking data. The vertical grey bars indicate time periods without eclipses

highly useful strategy for fitting the integrated orbit to the tracking data. The true aerodynamic acceleration will exhibit such 1 cycle-per-revolution (CPR) accelerations as well, for instance due to the sampling of the diurnal density variation over a circular noon-midnight orbit. In many cases however, higher frequency variations are important in the aerodynamic accelerations as well. It is therefore more accurate, if the density of the tracking data allows it, to estimate piecewise constant or piecewise linear accelerations over intervals much shorter than the orbital period, in order to resolve the variation of the acceleration within the orbit. This strategy is applied by van den IJssel and Visser [37–39].

4.3.3 Estimating Accelerometer Calibration Parameters

The final force model parameterisation scheme discussed here is slightly different. It involves the use of accelerometer observations in the orbit determination process. As already mentioned in Sect. 4.2.1, the raw accelerometer observations often exhibit acceleration biases and scale errors. These can be solved by including them as force model parameters in the orbit determination, and disabling all non-gravitational force models in the software.

If the parameters p_s and p_b represent the scale factors and biases, respectively, and the indices x, y and z denote the three orthogonal axes of the accelerometer instrument, then the non-gravitational forces in the orbit determination software can be parameterised and implemented as follows:

$$\ddot{\boldsymbol{r}}_\mathrm{a} \approx (p_{\mathrm{s,x}}\ddot{r}_{\mathrm{raw,x}} + p_{\mathrm{b,x}})\hat{\boldsymbol{u}}_\mathrm{x} + (p_{\mathrm{s,y}}\ddot{r}_{\mathrm{raw,y}} + p_{\mathrm{b,y}})\hat{\boldsymbol{u}}_\mathrm{y} + (p_{\mathrm{s,z}}\ddot{r}_{\mathrm{raw,z}} + p_{\mathrm{b,z}})\hat{\boldsymbol{u}}_\mathrm{z} \quad (4.37)$$

Note that the same caveat about the correlation between the along-track and radial acceleration components discussed above applies here. In addition, there also exists a correlation between the bias and the scale factor. According to the perturbation equations (Sect. 3.3), the effect of a constant acceleration component is much stronger than that of variations about the mean acceleration. As a result, there is a tendency to arrive at values for the pair of scale factor and bias which results in the correct mean acceleration over the arc, but with errors in the individual parameters.

For CHAMP and GRACE, the scale factor is therefore considered a constant for each accelerometer axis, or its value is determined by combining observations over much longer time intervals. Details on such strategies are provided by Van Helleputte et al. [35].

Figure 4.12 shows the time series of calibration biases $p_{\mathrm{b,x}}$, estimated from GPS data for CHAMP, as described by Van Helleputte et al. [35]. The scale factor was held fixed at a value of $p_{\mathrm{s,x}} = 0.8332$. The time series shows a general trend, of the order of 50 $\mathrm{nm/s^2/year}$, as well as large jumps, for example in mid 2001, early 2003 and early 2004. These jumps can be attributed to software updates and hardware switches onboard the satellite. Other excursions with similar signatures but different amplitudes occur at several of the periods where the satellite was in a dawn/dusk orbit and did not encounter eclipses, indicated by the grey bars in the plot. These jumps might be interpreted as signs that the accelerometer instrument is sensitive to variations in its thermal environment.

References

1. Bowman BR (2002) True satellite ballistic coefficient determination for HASDM. In: AIAA/AAS astrodynamics specialist conference and exhibit, 5–8 August 2002, Monterey, California, AIAA 2002–4887
2. Bowman BR, Moe K (2005) Drag coefficient variability at 175–500 km from the orbit decay analyses of spheres. In: AAS/AIAA astrodynamics specialist conference, 7–11 August 2005, Lake Tahoe, CA, AAS 05–257
3. Brouwer D (1959) Solution of the problem of artificial satellite theory without drag. Astron J 64(1274):378–397
4. Bruinsma S, Tamagnan D, Biancale R (2004) Atmospheric densities derived from CHAMP/STAR accelerometer observations. Planet Space Sci 52(4):297–312. doi:10.1016/j.pss.2003.11.004
5. Bruinsma S, Biancale R (2003) Total densities derived from accelerometer data. J Spacecraft Rockets 40(2):230–236
6. Bruinsma SL, Forbes JM (2007) Global observation of travelling atmospheric disturbances (TADs) in the thermosphere. Geophys Res Lett 34(L14103). doi:10.1029/2007GL030243
7. Bruinsma SL, Forbes JM (2008) Medium- to large-scale density variability as observed by CHAMP. Space Weather 6:S08002. doi:10.1029/2008SW000411
8. Bruinsma SL, Forbes JM (2009) Properties of traveling atmospheric disturbances (TADs) inferred from CHAMP accelerometer observations. Advan Space Res 43(3):369–376. doi:10.1016/j.asr.2008.10.031
9. Bruinsma SL, Forbes JM (2010) Anomalous behavior of the thermosphere during solar minimum observed by CHAMP and GRACE. J Geophys Res 115(A11323). doi:10.1029/2010JA015605
10. Burke WJ, Lin CS, Hagan MP, Huang CY, Weimer DR, Wise JO, Gentile LC, Marcos FA (2009) Storm time global thermosphere: a driven-dissipative thermodynamic system. J Geophys Res 114(A06306) doi:10.1029/2008JA013848

11. Case K, Kruizinga GLH, Wu SC (2004) GRACE level 1B data product user handbook. JPL D-22027
12. Cefola PJ, Nazarenko AI, Proulx RJ, Yurasov VS (2003) Atmospheric density correction using two line element sets as the observation data. In: AAS/AIAA astrodynamics specialists conference, 3–7 August 2003, Big Sky, Montana, AAS 03–626
13. Doornbos E, Scharroo R, Klinkrad H, Zandbergen R, Fritsche B (2002) Improved modelling of surface forces in the orbit determination of ERS and Envisat. Can J Remote Sens 28(4):535–543
14. Doornbos E (2006) NRTDM final report—Near Real-Time Density Model (NRTDM)—ESOC contract 18576/04/D/HK(SC). Delft Institute for Earth-Oriented Space Research
15. Doornbos E, Klinkrad H, Scharroo R, Visser P (2007) Thermosphere density model calibration in the orbit determination and prediction of ERS-2 and Envisat. In: Lacoste H (ed) Envisat symposium 23–27 April 2007. Montreux, Switzerland, ESA SP-636
16. Doornbos E, Klinkrad H, Visser P (2008) Use of two-line element data for thermosphere neutral density model calibration. Advan Space Res 41(7):1115–1122. doi:10.1016/j.asr.2006.12.025
17. Doornbos E, Förster M, Fritsche B, Helleputte T van, IJssel J van den, Koppenwallner G, Lühr H, Rees D, Visser P (2009) ESTEC contract 21022/07/NL/HE Air density models derived from multi-satellite drag observations—final report. DEOS / TU Delft scientific report 01/2009, TU Delft
18. Doornbos E, Van den IJsse J, Lühr H, Förster M, Koppenwallner G (2010) Neutral density and crosswind determination from arbitrarily oriented multiaxis accelerometers on satellites. J Spacecraft Rockets 47(4):580–589. doi:10.2514/1.48114
19. Drob DP, Emmert JT, Crowley G, Picone JM, Shepherd GG, Skinner W, Hays P, Niciejewski RJ, Larsen M, She CY, Meriwether JW, Hernandez G, Jarvis MJ, Sipler DP, Tepley CA, O'Brien MS, Bowman JR, Wu Q, Murayama Y, Kawamura S, Reid IM, Vincent RA (2008) An empirical model of the earth's horizontal wind fields: HWM07. J Geophys Res 113(A12304). doi:10.1029/2008JA013668
20. Emmert JT (2009) A long-term data set of globally averaged thermospheric total mass density. J Geophys Res 114(A06315). doi:10.1029/2009JA014102
21. Emmert JT, Picone JM (2010) Climatology of globally averaged thermospheric mass density. J Geophys Res 115(A09326). doi:10.1029/2010JA015298
22. Emmert JT, Picone JM, Lean JL, Knowles SH (2004) Global change in the thermosphere: Compelling evidence of a secular decrease in density. J Geophy Res 109(A2):A02301. doi:10.1029/2003JA010176
23. Emmert JT, Meier RR, Picone JM, Lean JL, Christensen AB (2006) Thermospheric density 2002–2004: TIMED/GUVI dayside limb observations and satellite drag. J Geophys Res 111(A10S16). doi:10.1029/2005JA011495
24. Emmert JT, Picone JM, Meier RR (2008) Thermospheric global average density trends, 1967–2007, derived from orbits of 5,000 near-earth objects. Geophys Res Lett 35(L05101). doi:10.1029/2007GL032809
25. Flury J, Bettadpur S, Tapley BD (2008) Precise accelerometry onboard the GRACE gravity field satellite mission. Advan Space Res 42(8):1414–1423. doi:10.1016/j.asr.2008.05.004
26. Forbes JM, Lu G, Bruinsma S, Nerem S, Zhang X (2005) Thermosphere density variations due to the 15–24 April 2002 solar events from CHAMP/STAR accelerometer measurements. J Geophys Res 110(A12S27). doi:10.1029/2004JA010856
27. Forbes JM, Bruinsma SL, Miyoshi Y, Fujiwara H (2008) A solar terminator wave in thermosphere neutral densities measured by the CHAMP satellite. Geophys Res Lett 35(L14802). doi:10.1029/2008GL034075
28. Forbes JM, Bruinsma SL, Zhang X, Oberheide J (2009) Surface-exosphere coupling due to thermal tides. Geophys Res Lett 36(L15812). doi:10.1029/2009GL038748
29. Förste Ch (2002) Format description: The CHAMP data format. CH-GFZ-FD-001
30. Förster M, Rentz S, Köhler W, Liu H, Haaland SE (2008) IMF dependence of high-latitude thermospheric wind pattern derived from CHAMP cross-track measurements. Ann Geophys 26(6):1581–1595

31. Förster M, Doornbos E, Van Helleputte T , Haaland SE, Rentz S, Lühr H (2009) Magnetic forcing of the high-latitude upper atmosphere. In: Proceedings of ESA's second swarm international science meeting, 24–26 June 2009, Potsdam, Germany
32. Guo J, Wan W, Forbes JM, Sutton E, Nerem RS, Woods TN, Bruinsma S, Liu L (2007) Effects of solar variability on thermosphere density from CHAMP accelerometer data. J Geophys Res 112(A10308). doi:10.1029/2007JA012409
33. Häusler K, Lühr H (2009) Nonmigrating tidal signals in the upper thermospheric zonal wind at equatorial latitudes as observed by CHAMP. Ann Geophys 27(6):2643–2652
34. Häusler K, Lühr H, Rentz S, Köhler W (2007) A statistical analysis of longitudinal dependencies of upper thermospheric zonal winds at dip equator latitudes derived from CHAMP. J Atmos Solar-Terr Phys 69(12):1419–1430. doi:10.1016/j.jastp.2007.04.004
35. Helleputte T. van, Doornbos E, Visser P (2009) CHAMP and GRACE accelerometer calibration by GPS-based orbit determination. Advan Space Res 43(12):1890–1896. doi:10.1016/j.asr.2009.02.017
36. Hoots FR, Roehrich RL (1980) Spacetrack report no. 3: models for propagation of NORAD element sets. Aerospace Defense Center Peterson Air Force Base. Obtained from http://www.celestrak.com/
37. van den IJssel J, Visser P (2005) Determination of non-gravitational accelerations from GPS satellite-to-satellite tracking of CHAMP. Advan Space Res 36(3):418–423. doi:10.1016/j.asr.2005.01.107
38. van den IJssel J, Visser P (2007) Performance of GPS-based accelerometry: CHAMP and GRACE. Advan Space Res 39(10):1597–1603. doi:10.1016/j.asr.2006.12.027
39. van den IJssel J, Visser P (2010) Performance of gps-based accelerometry: a simulation experimen. Advan Space Res 45(2):225–238. doi:10.1016/j.asr.2009.09.012
40. Keating GM, Tolson RH, Bradford MS (2000) Evidence of long term global decline in the earth's thermospheric densities apparently related to anthropogenic effects. Geophys Res Lett 27(10):1523–1526
41. King-Hele D (1987) Satellite orbits in an atmosphere, theory and applications. Blackie, Glasgow
42. König R, Michalak G, Neumayer KH, Schmidt R, Zhu SY, Meixner H, Reigber C (2005) Recent developments in CHAMP orbit determination at GFZ. In: Earth observation with CHAMP, results from three years in orbit. pp 65–70
43. Lane MH, Cranford KH (1969) An improved analytical drag theory for the artificial satellite problem. In: Astrodynamics conference, 20–22 August 1969 AIAA. Princeton, NJ, number AIAA 69–925
44. Lathuillère C, Menvielle M (2010) Comparison of the observed and modeled low- to mid-latitude thermosphere response to magnetic activity: effects of solar cycle and disturbance time delay. Advan Space Res 45(9):1093–1100. doi:10.1016/j.asr.2009.08.016
45. Lathuillère C, Menvielle M, Marchaudon A, Bruinsma S (2008) A statistical study of the observed and modeled global thermosphere response to magnetic activity at middle and low latitudes. J Geophys Res 113(A07311). doi:10.1029/2007JA012991
46. Lean JL, Picone JM, Emmert JT, Moore G (2006) Thermospheric densities derived from spacecraft orbits: application to the Starshine satellites. J Geophys Res 111(A04301). doi:10.1029/2005JA011399
47. Lei J, Thayer JP, Forbes JM, Sutton EK, Nerem RS, Temmer M, Veronig AM (2008) Global thermospheric density variations caused by high-speed solar wind streams during the declining phase of solar cycle 23. J Geophys Res 113(A11303). doi:10.1029/2008JA013433
48. Liu H, Lühr H (2005) Strong disturbances of the upper thermospheric density due to magnetic storms: CHAMP observations. J Geophys Res 110(A09829). doi:10.1029/2004JA010908
49. Liu H, Lühr H, Henize V, Köhler W (2005) Global distribution of the thermospheric total mass density derived from CHAMP. J Geophys Res 110(A04301) doi:10.1029/2004JA010741

50. Liu H, Lühr H, Watanabe S, Köhler W, Henize V, Visser P (2006) Zonal winds in the equatorial upper thermosphere: decomposing the solar flux, geomagnetic activity, and seasonal dependencies. J Geophys Res 111(A07307). doi:10.1029/2005JA011415
51. Liu H, Lühr H, Watanabe S (2007a) Climatology of the equatorial thermospheric mass density anomaly. J Geophys Res 112(A05305). doi:10.1029/2006JA012199
52. Liu H, Lühr H, Watanabe S, Köhler W, Manoj C (2007b) Contrasting behavior of the thermosphere and ionosphere in response to the 28 Oct 2003 solar flare. J Geophys Res 112(A077305), doi:/10.1029/2007JA012313
53. Liu H, Lühr H, Watanabe S (2009) A solar terminator wave in thermospheric wind and density simultaneously observed by CHAMP. Geophys Res Lett 36(L10109). doi:10.1029/2009GL038165
54. Liu R, Lühr H, Doornbos E, Ma S-Y (2010) Thermospheric mass density variations during geomagnetic storms and a predicition model based on the merging electric field. Ann Geophys 28:1633–1645. doi:10.5194/angeo-28-1633-2010
55. Lühr H, Rother M, Köhler W, Ritter P, Grunwaldt L (2004) Thermospheric upwelling in the cusp region: evidence from CHAMP observations. Geophys Res Lett 31(6) doi:10.1029/2003GL019314
56. Lühr H., Rentz S., Ritter P., Liu H., Häusler K (2007a) Average thermospheric wind pattern over the polar regions, as observed by CHAMP. Ann Geophys 25(5):1093–1101
57. Lühr H, Häusler K, Stolle C (2007b) Longitudinal variation of F region electron density and thermospheric zonal wind caused by atmospheric tides. Geophys Res Lett 34(L16102). doi:10.1029/2007GL030639
58. Ma R, Xu J, Wang W, Lei J, Liu H-L, Maute A, Hagan ME (2010) Variations of the night-time thermospheric mass density at low and middle latitudes. J Geophys Res 115(A12301). doi:10.1029/2010JA015784
59. Marcos FA, Forbes JM (1985) Thermospheric winds from the satellite electrostatic triaxial accelerometer system. J Geophys Res 90:6543–6552
60. McCarthy DD, Petit G (2003) IERS conventions (2003). IERS technical note, no. 32. International Earth Rotation and Reference Systems Service (IERS)
61. Menvielle M, Lathuillère C, Bruinsma S, Viereck R (2007) A new method for studying the thermospheric density variability derived from CHAMP/STAR accelerometer data for magnetically active conditions. Ann Geophys 25:1949–1958
62. Miyoshi Y, Fujiwara H, Forbes JM, Bruinsma SL (2009) Solar terminator wave and its relation to the atmospheric tide. J Geophys Res 114(A07303). doi:10.1029/2009JA014110
63. Montenbruck O, Gill E (2000) Satellite orbits models, methods and applications. Springer, Berlin
64. Müller S, Lühr H, Rentz S (2009) Solar and magnetospheric forcing of the low latitude thermospheric mass density as observed by CHAMP. Ann Geophys 27(5):2087–2099
65. Oberheide J, Forbes JM, Häusler K, Wu Q, Bruinsma SL (2009) Tropospheric tides from 80 to 400 km: propogation, interannual variability, and solar cycle effects. J Geophys Res 114(D00I05). doi:10.1029/2009JD012388
66. Pardini C, Anselmo L (1994) SATRAP: satellite reentry analysis program. Internal Report C94-17, Istituto CNUCE, CNR, Pisa, 30 Agosto 1994
67. Pardini C, Anselmo L, Moe K, Moe MM (2010) Drag and energy accommodation coefficients during sunspot maximum. Advan Space Res 45(5):638–650. doi:10.1016/j.asr.2009.08.034
68. Perosanz R (2003) On board evaluation of the STAR accelerometer. In: Christoph R et al.(eds) First CHAMP mission results for gravity magnetic and atmospheric studies, Springer, Berlin, pp 11–18
69. Picone JM, Hedin AE, Drob DP, Aikin AC (2002) NRLMSISE-00 empirical model of the atmosphere: statistical comparisons and scientific issues. J Geophys Res 107(A12). doi:10.1029/2002JA009430

70. Picone JM, Emmert JT, Lean J (2005) Thermospheric densities derived from spacecraft orbits-I. Accurate processing of two-line element sets. J Geophys Res 110(A03301). doi:10.1029/2004JA010585
71. Pilinski MD, Argrow BM, Palo SE (2011) Drag coefficients of satellites with concave geometries: comparing models and observations. J Spacecraft Rockets 48(2):312–324
72. Rentz S, Lühr H (2008) Climatology of the cusp-related thermospheric mass density anomaly, as derived from CHAMP observations. Ann Geophys 26(9):2807–2823
73. Ritter P, Lühr H, Doornbos E (2010) Substorm-related thermospheric density and wind disturbances derived from CHAMP observations. Ann Geophys 28:1207–1220. doi:10.5194/angeo-28-1207-2010
74. Sutton EK, Forbes JM, Nerem RS (2005) Global thermospheric neutral density and wind response to the severe 2003 geomagnetic storms from CHAMP accelerometer data. J Geophys Res 110(A09S40). doi:10.1029/2004JA010985
75. Sutton EK, Forbes JM, Knipp DJ (2009) Rapid response of the thermosphere to variations in joule heating. J Geophys Res 114(A04319). doi:10.1029/2008JA013667
76. Sutton EK, Nerem RS, Forbes JM (2007) Density and winds in the thermosphere deduced from accelerometer data. J Spacecraft Rockets 44(6):1210–1219. doi:10.2514/1.28641
77. Tapley BD, Schutz BE, Born GH (2004) Statistical orbit determination. Elsevier Academic, New York
78. Tapley BD, Ries JC, Bettadpur S, Cheng M (2007) Neutral density measurements from the gravity recovery and climate experiment accelerometers. J Spacecraft Rockets 6(44):1220–1225. doi:10.2514/1.28843
79. Touboul P, Foulon B, Rodrigues M, Marque JP (2004) In orbit nano-g measurements, lessons for future space missions. Aerosp Sci Technol (8):431–441
80. Vallado DA (2001) Fundamentals of astrodynamics and applications, 2nd edn. Microcosm Press, El Segundo
81. Vallado DA, Crawford P (2008) SGP4 orbit determination. In: 2008 AIAA/AAS astrodynamics specialist conference
82. Vallado DA, Crawford P, Hujsak R, Kelso TS (2006) Revisiting spacetrack report ♯3. In: AIAA astrodynamics specialists conference and exhibit, AIAA 2006–6753